NASA/TM-20220012716

Assessment of Gaseous Helium Cooling in a Superconducting Coil Test Rig

Gerald V. Brown and Benjamin B. Choi
Glenn Research Center, Cleveland, Ohio

Kirsten P. Duffy
University of Toledo, Toledo, Ohio

Jason W. Hartwig
Glenn Research Center, Cleveland, Ohio

David S. Hervol, Paul J. Passe, and Frederick W. Van Keuls
HX5, LLC, Brook Park, Ohio

August 2023

NASA STI Program . . . in Profile

Since its founding, NASA has been dedicated to the advancement of aeronautics and space science. The NASA Scientific and Technical Information (STI) Program plays a key part in helping NASA maintain this important role.

The NASA STI Program operates under the auspices of the Agency Chief Information Officer. It collects, organizes, provides for archiving, and disseminates NASA's STI. The NASA STI Program provides access to the NASA Technical Report Server—Registered (NTRS Reg) and NASA Technical Report Server—Public (NTRS) thus providing one of the largest collections of aeronautical and space science STI in the world. Results are published in both non-NASA channels and by NASA in the NASA STI Report Series, which includes the following report types:

- TECHNICAL PUBLICATION. Reports of completed research or a major significant phase of research that present the results of NASA programs and include extensive data or theoretical analysis. Includes compilations of significant scientific and technical data and information deemed to be of continuing reference value. NASA counter-part of peer-reviewed formal professional papers, but has less stringent limitations on manuscript length and extent of graphic presentations.

- TECHNICAL MEMORANDUM. Scientific and technical findings that are preliminary or of specialized interest, e.g., "quick-release" reports, working papers, and bibliographies that contain minimal annotation. Does not contain extensive analysis.

- CONTRACTOR REPORT. Scientific and technical findings by NASA-sponsored contractors and grantees.

- CONFERENCE PUBLICATION. Collected papers from scientific and technical conferences, symposia, seminars, or other meetings sponsored or co-sponsored by NASA.

- SPECIAL PUBLICATION. Scientific, technical, or historical information from NASA programs, projects, and missions, often concerned with subjects having substantial public interest.

- TECHNICAL TRANSLATION. English-language translations of foreign scientific and technical material pertinent to NASA's mission.

For more information about the NASA STI program, see the following:

- Access the NASA STI program home page at http://www.sti.nasa.gov

- E-mail your question to help@sti.nasa.gov

- Fax your question to the NASA STI Information Desk at 757-864-6500

- Telephone the NASA STI Information Desk at 757-864-9658

- Write to:
  NASA STI Program
  Mail Stop 148
  NASA Langley Research Center
  Hampton, VA 23681-2199

NASA/TM-20220012716

Assessment of Gaseous Helium Cooling in a Superconducting Coil Test Rig

Gerald V. Brown and Benjamin B. Choi
Glenn Research Center, Cleveland, Ohio

Kirsten P. Duffy
University of Toledo, Toledo, Ohio

Jason W. Hartwig
Glenn Research Center, Cleveland, Ohio

David S. Hervol, Paul J. Passe, and Frederick W. Van Keuls
HX5, LLC, Brook Park, Ohio

National Aeronautics and
Space Administration

Glenn Research Center
Cleveland, Ohio 44135

August 2023

This work was sponsored by the Advanced Air Vehicle Program
at the NASA Glenn Research Center

Level of Review: This material has been technically reviewed by technical management.

This report is available in electronic form at https://www.sti.nasa.gov/ and https://ntrs.nasa.gov/

Assessment of Gaseous Helium Cooling in a Superconducting Coil Test Rig

Gerald V. Brown and Benjamin B. Choi
National Aeronautics and Space Administration
Glenn Research Center
Cleveland, Ohio 44135

Kirsten P. Duffy
University of Toledo
Toledo, Ohio 43606

Jason W. Hartwig
National Aeronautics and Space Administration
Glenn Research Center
Cleveland, Ohio 44135

David S. Hervol, Paul J. Passe, and Frederick W. Van Keuls
HX5, LLC
Brook Park, Ohio 44142

Summary

An experimental rig was designed and constructed at the NASA Glenn Research Center to measure the alternating current (AC) losses of round, multifilament, superconducting (SC), magnesium diboride (MgB_2) wire in the temperature range from 20 to 30 K. The rig resembles a permanent magnet (PM) motor with the stator windings omitted. Experiment packs containing the superconductor samples will be placed in the annular space between the rotor and the stator back iron. The original plan was to measure the AC losses by calorimetry using nonboiling liquid hydrogen as the cooling fluid. The present plan is to use helium gas (GHe) under a few bar pressure instead. This report summarizes the calculations that indicate that reasonable results can be obtained, even though the mass density of the GHe will be only a fraction of that of liquid hydrogen. It is necessary to show that the heat transfer coefficient from SC wire to GHe can be high enough, that the temperature rise of the He between the experiment inlet and outlet can be small enough, and that sufficient He flow can be driven by a commercially available He fan. Both straight wire samples to validate loss models and coils to simulate motor stator coils can be tested in the rig. The lowest superconductor temperature that is feasible to reach in the rig is estimated. The temperature range available for samples will be wider with the gaseous He system than it would have been with liquid hydrogen.

Introduction

The NASA Glenn Research Center is evaluating fully superconducting (SC) electric machines as possible components in the propulsion powertrain of a large transport aircraft with distributed electric propulsion. Reducing the alternating current (AC) losses in the stator coils of the fully SC machines is a central problem for that application. NASA has been supporting the development of a low-AC-loss magnesium diboride (MgB_2) superconductor for several years (e.g., see Hyper Tech Research, 2013 and

2019 unpublished). To measure the AC losses in coils of such wire, Glenn has followed the lead of the Air Force Research Laboratory (AFRL) (Haugan, 2015 unpublished; and Murphy et al., 2013, 2015, 2017) in designing a rig to measure the losses in a realistic stator-coil environment. AFRL has used their rig to measure losses in high-temperature superconductors, but it is necessary to extend the temperature range to between 20 and 30 K to take advantage of the much lower AC losses in multifilament, round-wire, MgB_2 superconductors. Therefore, the Glenn team copied the AFRL rotor exactly but included a larger space between the rotor and the back iron to allow more room to create a variable temperature environment to test samples down to 20 K, even though field uniformity is reduced to some degree. The team originally considered using liquid hydrogen as the calorimetric fluid, to be passed through once and exhausted, as AFRL did with LN_2, but the plan was changed to use helium gas (GHe) in a closed circulating loop in order to reduce cost, enlarge the available temperature range, and reduce safety and programmatic risks. The change was made after the design of the core rig itself was frozen and fabrication was well under way. The as-built rig is described in the report by Hartwig et al. (2019). The calculations summarized in this report were made to verify that the change to GHe as the calorimetric fluid can be expected to yield good AC loss measurements.

AC loss measurements on spatially extended SC samples, whether coils or straight conductors, have some issues associated with them. The applied magnetic field strength will vary with position over the SC sample, as will the temperature of the GHe calorimetric fluid. The Glenn team will not perform integrations of various quantities over regions of varying field and fluid temperatures until actual experimental data are available for comparison. Rather, the numerical results presented herein are based on chosen single values of field and superconductor temperature. Furthermore, in the experiment, no direct measurement of superconductor temperature will be feasible, so superconductor temperature must be inferred from measured fluid temperatures and models of fluid flow and heat transfer.

This report begins with the relevant SC properties of MgB_2, namely, its current carrying capacity and the AC losses expected under the operating conditions. Next, the design of the experiment pack is discussed, along with the planned GHe circulation system. Then, a typical operating condition is defined and the consequent expected experimental results are discussed. The results of interest are the expected superheat of the superconductor above the temperature of the coolant fluid, the amount of heating of the fluid from the inlet to the outlet, the pressure drop expected in the coolant channels and the other parts of the closed cooling loop, and the range of SC sample temperatures that will be accessible in the rig.

Superconductor Properties and Loss-Prediction Approach

For the superconductor geometry and regime of interest, the main losses are anticipated to be the hysteresis loss and the coupling loss, which depend on the amplitude, frequency, and ellipticity of the applied magnetic field, on the basic superconductor properties, and on several superconductor configuration parameters. The main superconductor material property that affects the losses is the critical current density, which is a function of temperature and applied field. The configuration parameters of interest of the multifilament SC wire are the wire diameter, the filament diameter, the filament twist pitch, and the effective transverse resistivity of the metallic matrix of the wire. The parameter values for the Example Case are listed in Table 1.

TABLE 1.—EXAMPLE CASE PARAMETERS FOR TWO COILS IN HYDRAULIC SERIES

Hydraulic diameter of channels, mm	0.75
Fluid velocity in cooling channels, m/s	8
B_{ro} (major semiaxis), T	0.50
B_{tano} (minor semiaxis), T	0.30
Frequency, Hz	200
T_{mean} of superconductor, K	25
Inlet pressure, bar	4
Wire diameter, mm	0.85
MgB_2 filament diameter, μm	31
SC filament twist pitch, mm	10
Superconductor volume fraction	0.12
Effective transverse resistivity of matrix, μΩ-cm	13.8
Channel length, each coil (two coils in hydraulic series), cm	20
Number of turns in each coil	16
Number of parallel channels	34
Assumed tare heat leak, W	2.0

The critical current density J_c (in A/mm^2) in the SC filaments, as a function of the temperature T and the magnetic field B, which was used to predict the hysteresis losses, is a data fit made from data provided in Hyper Tech (2013 unpublished):

$$J_c = (-4.4 + 1.6 * B) * T^2 - (60.4 + 73.6 * B) * T + (7966 - 966 * B) \quad (1)$$

which is valid for $0 \le B \le 1$ T and 20 K $\le T \le$ 30 K. This expression represents the critical current density over the range of temperature and field strengths expected in the coil tester rig better than the expression used in Brown et al. (2020), which was originally derived anticipating that somewhat higher strength magnetic fields might be required. See Appendix A for further comparison.

Figure 1 is a contour plot of J_c in the filaments as a function of T and B; Figure 2 plots J_c on a whole-wire basis (for 12 percent superconductor packing fraction). Note, for example, from Figure 1 that at 25 K and 0.5 T, the filaments can carry 2,800 A/mm^2 and from Figure 2 that the wire can carry 330 A/mm^2. Figure 3 shows the temperature dependence of the filament critical current density. Note that from the example condition at 25 K, the critical current density falls from 2,800 to 1,400 A/mm^2 at 30 K or rises to 4,100 A/mm^2 at 20 K. The value at 20 K is almost 3 times that at 30 K, which will be seen to produce predicted hysteresis losses that are almost 3 times as much at 20 K as at 30 K.

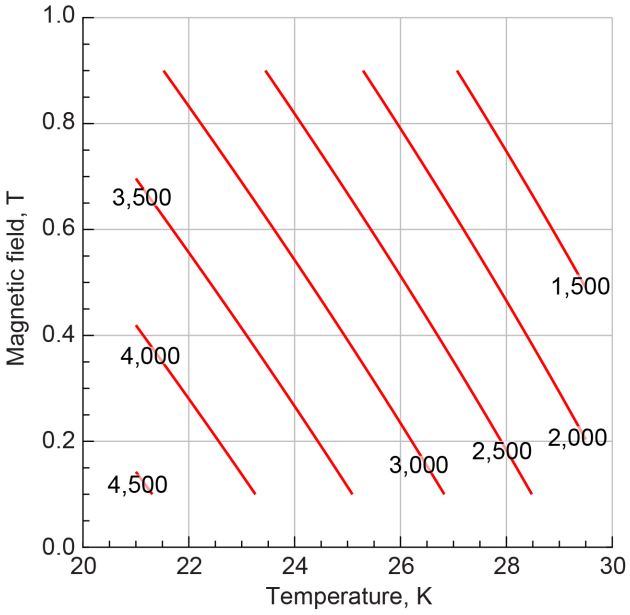

Figure 1.—Critical current density in filaments (in A/mm^2) of MgB_2 multifilamentary wire as function of temperature and magnetic field.

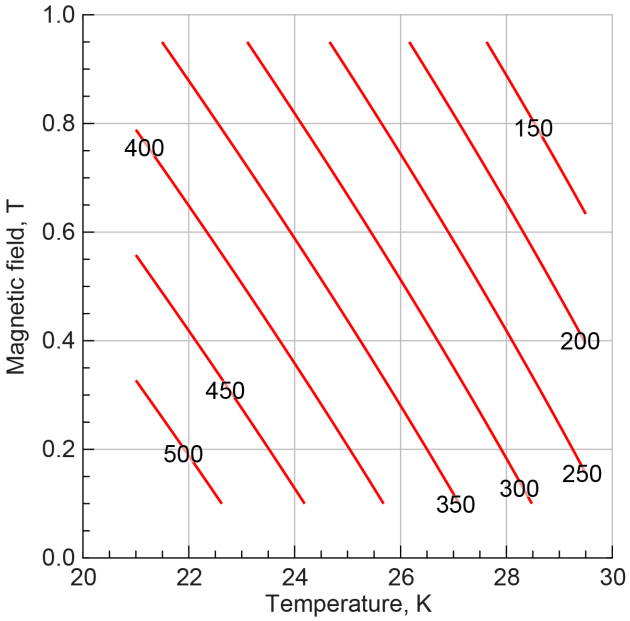

Figure 2.—Critical current density (in A/mm^2) of MgB_2 strands as function of temperature and magnetic field.

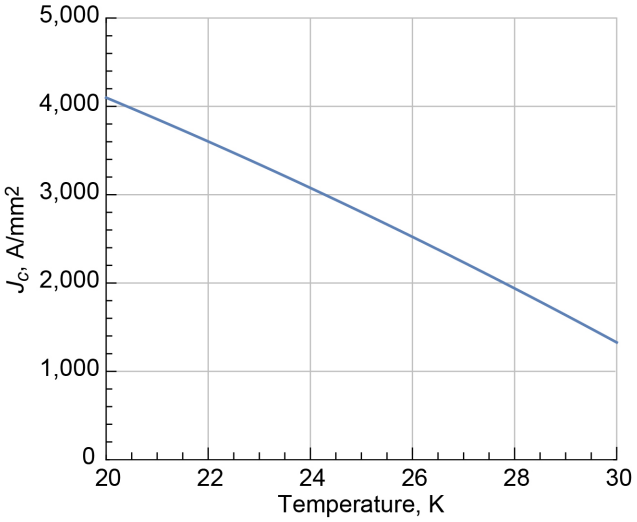

Figure 3.—Critical current density in filaments at 0.5 T as function of temperature.

Strength and Nature of Magnetic Field

Before estimating the expected AC losses, it is necessary to know the nature of the local magnetic field at points along the SC wires. The field is produced by an 8-pole array of permanent magnets (PMs)with fourfold rotational symmetry and a constant cross section along its 8-in. (0.203-m) length. Consequently, the magnetic field has reflective symmetry about the plane (hereinafter referred to as the "midplane") that is perpendicular to the axis and midway between the ends of the array. Figure 4 is a cross-sectional drawing of the assembly of rotor magnets, their containment shell, the annular space in which experiments can be mounted, an experiment pack with two racetrack coils at different radial locations, and the inner and outer surfaces of the back iron. The collection of rotor magnets is similar to a Halbach configuration, but with longer, radially magnetized pieces and with inner back iron. The apparent space behind the experiment pack (shown in green) is not all available for use presently because of unshown obstructions, but it could be later. Figure 5 shows the strength of the two field components in the midplane of the rotor, at the average radius of each of the coils, as functions of the angular orientation of the rotor. The field components are plotted in the B_r versus B_{tan} plane in Figure 6. It can be seen that the field has a purely oscillatory character (orange curve) only at the surface of the back iron, where the field must be purely radial because the iron is well below saturation. At the radial locations of the two experimental coils, the field orbit is rather elliptical, and it has a somewhat rounded and pinched rectangular appearance near the surface of the rotor shell. At the location of the SC coils, the roughly elliptical character of the magnetic field affects the hysteretic AC losses in a complicated way, as examined by Lorin and Masson (2013). The Glenn team will not utilize that approach, however, but will take a simpler, upper-bounding approach by calculating the hysteresis loss for a purely rotating field with a field strength set equal to that of the radial field amplitude. At the midplane, the amplitude of the radial field component is 0.51 T at the inner coil radius and 0.41 T at the outer coil radius, and the amplitude of the tangential component is 0.33 T at the inner coil radius and 0.21 T at the outer coil radius. The maximum amplitude of the axial component occurs near the endplane of the magnet assembly and is 0.33 T at the inner coil radius and 0.21 T at the outer coil radius.

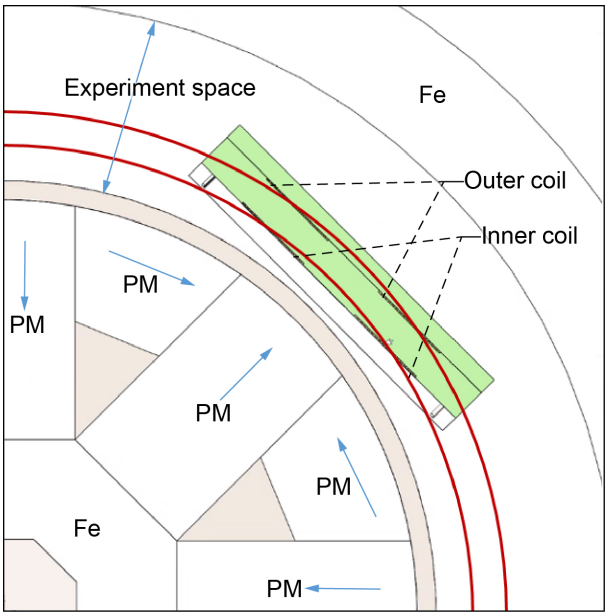

Figure 4.—Section through axial midplane of magnet system, showing magnets, containment shell, experimental conductor pack (green), and back iron. Dark red arcs indicate average radii from rotor axis of each coil.

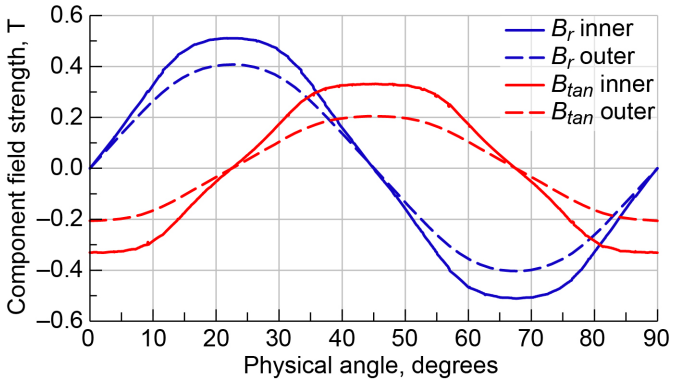

Figure 5.—Magnetic field components in axial midplane at average radii of inner coil wires (16.5 cm) and of outer coil wires (17.6 cm) as functions of angular position around rotor.

Next, consider how the amplitude of each field component varies with axial distance from the magnet midplane. These amplitudes are plotted in Figure 7. From its maximum midplane value of 0.51 T at the inner coil radius, the radial field component falls to 0.27 at the magnet endplane, which is 10.2 cm (4 in.) from the midplane. At the outer coil radius, the radial field falls from 0.41 at the midplane to 0.21 at the endplane. The percentages by which the radial component amplitudes decrease from their midplane values are plotted in Figure 8 (right scale). It can be seen that the radial component amplitude drops by about 5 percent at 5 cm from the midplane.

The rate of decrease of the field outside the end of the magnets is also important because it affects losses in the end turns of sample coils and governs where metallic parts can be safely located without significant eddy current heating. It can be seen that the field drops to 0.01 T at about 7.47 cm (2.9 in.)

from the magnet endplane. It can be seen from Figure 7 that the amplitude of the axial component of the field is less than that of the other two field components except near the endplane of the magnets and beyond. Its contribution to losses in the end turns of experimental coils will have to be taken into account.

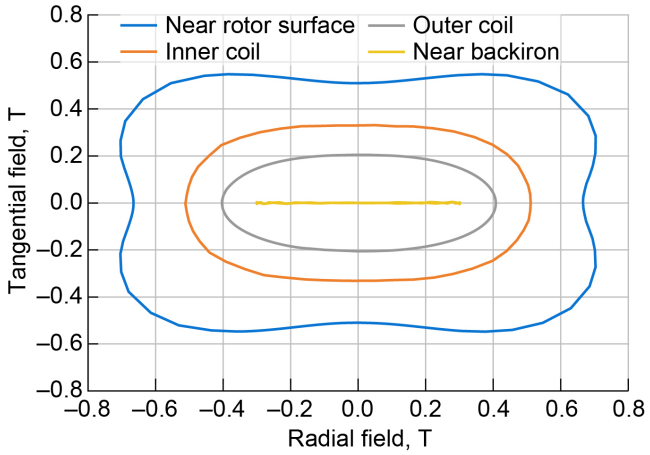

Figure 6.—Midplane field orbits at four radial locations.

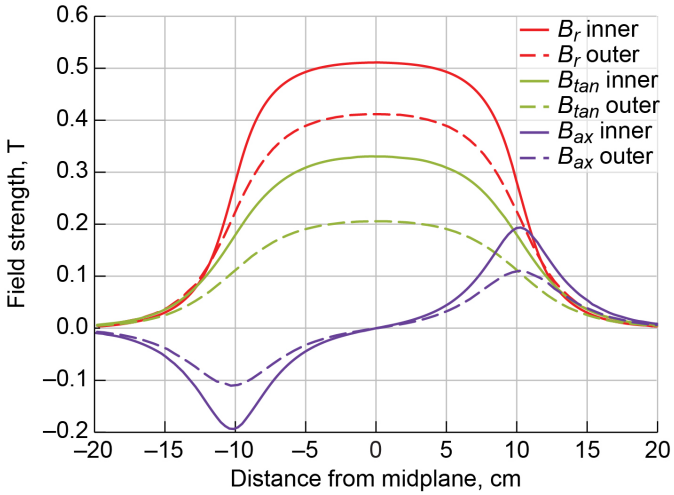

Figure 7.—Axial dependence of amplitudes of radial, axial, and tangential field components versus axial distance from midplane. Magnet endplanes are 10.2 cm from midplane.

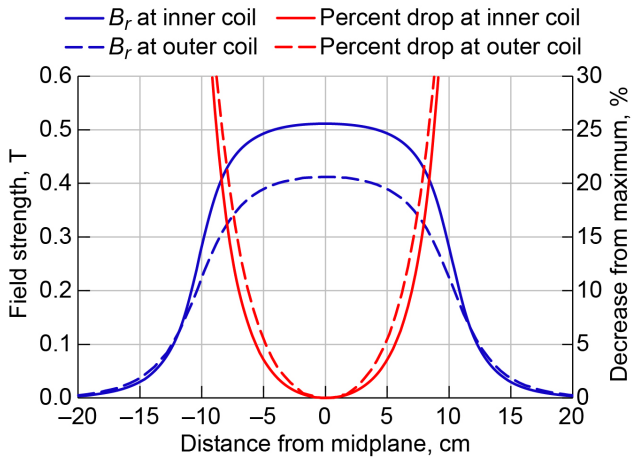

Figure 8.—Radial component amplitude at each coil as functions of axial distance from midplane (left scale) and associated percentage drop from midplane values (right scale).

Predicted AC Losses for MgB_2 Multifilament Round Wire

AC losses in the type of MgB_2 wire that will be used have been previously discussed in Brown et al. (2020). Fortunately, the field strength amplitude of 0.4 T at the outer coil position is far more than the full penetration field B_p for the SC filaments, as shown in Appendix B, so loss formulas are needed only for the full penetration field regime. For full penetration, the hysteresis loss P_h for a purely oscillating field is given by

$$P_{ho} = \left(\frac{8}{3\pi}\right) J_c B d f V_{\text{filaments}} \tag{2}$$

where B is the field amplitude, f is its frequency, d is the diameter of the SC filaments, and $V_{\text{filaments}}$ is the volume of the SC filaments. The hysteresis loss has a considerable dependence on temperature through the critical current density J_c. For a purely rotating field of magnitude B, the hysteresis loss is

$$P_{hr} = \left(\frac{4}{3}\right) J_c B d f V_{\text{filaments}} \tag{3}$$

As noted above, the actual nature of the magnetic field experienced by the superconductor in a machine stator is neither of these pure cases but something in between. For nonsinusoidal oscillatory waveforms, the hysteresis loss does not change with the waveform as long as the field changes monotonically between its extrema. To be conservative, the larger rotating field loss P_{hr} will be used in the estimates rather than the oscillating field loss

$$P_h = \left(\frac{4}{3}\right) J_c B d f V_{\text{filaments}} \tag{4}$$

where B will be set equal to the amplitude B_{ro} of the larger, radial-field component. The coupling loss P_c for a purely oscillating field of strength B is given by

$$P_c = \left(\frac{1}{2\,\rho_{eff}}\right)\left(BL_p f\right)^2 V_{\text{matrix}} \tag{5}$$

where ρ_{eff} is the effective transverse resistivity of the matrix (including the niobium tubes) in which the SC filaments are embedded, L_p is the twist pitch of the filaments (a full 360° of twist), and V_{matrix} is the volume of matrix material, including the niobium. The coupling loss does not have a strong dependence on temperature in a range where the matrix resistivity is reasonably constant, as is true at temperatures less than 30 K for a preferred matrix alloy such as CuNi. For the elliptical fields, the total coupling loss P_{ctot} will be estimated as if the two perpendicular components of the elliptical field are independent of each other. Therefore, Equation (5) will be applied to each component separately and then added together so the total coupling loss P_{ctot} is

$$P_{ctot} = \left(\frac{1}{2\,\rho_{eff}}\right)\left(B_{ro}^2 + B_{tano}^2\right)\left(L_p f\right)^2 V_{\text{matrix}} \tag{6}$$

where B_{tano} is the amplitude of the tangential component, and it is assumed that B_{ro} is larger than B_{tano}.

Wires with 12 percent superconductor and 88 percent matrix are considered (using the simplification that all nonsuperconducting material is matrix, even including the exterior sheath), so these losses can be translated into loss per total wire volume. That total coupling loss, plus the hysteresis loss per wire volume is plotted in Figure 9 as a function of frequency for three temperatures and two twist pitches. These experiments will offer access to frequencies from 0 to 400 Hz, but at very low frequencies where the loss is very low, the accuracy of the AC loss measurement will suffer. As will be noted later in this report, accuracy may suffer at high frequencies as well because, for high losses, the superconductor will be spread over a larger range of temperatures.

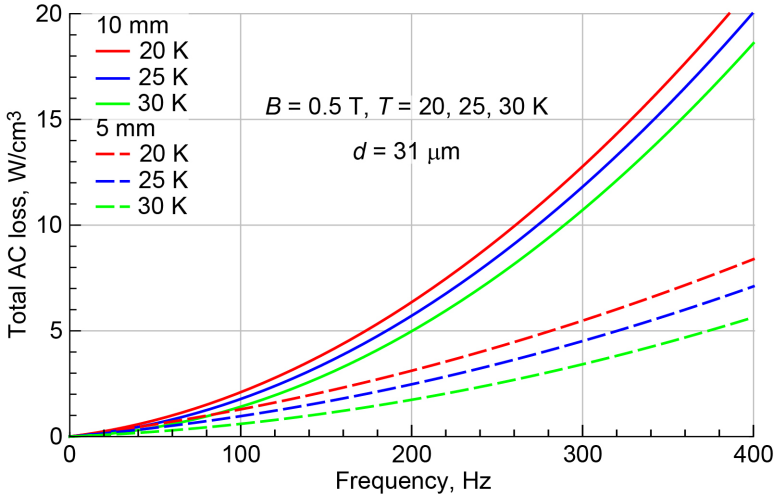

Figure 9.—Hysteresis plus coupling AC loss per wire volume for multifilament wire as function of frequency at three temperatures, 30 K (green), 25 K (blue), and 20 K (red), for two twist pitch values, 10 mm (solid curves) and 5 mm (dashed curves). All curves are for 0.5 T amplitude, β = 0.6, and SC filaments of 31-μm diameter.

It is interesting to know at what frequency the hysteresis loss and coupling loss are equal. At lower frequencies, the hysteresis loss is larger; at higher frequencies, the coupling loss is larger. Setting the expressions in Equations (4) and (6) equal and solving for f gives

$$f_{\text{crossover}} = \frac{8}{3}\rho_{eff}\frac{\alpha}{1-\alpha}\frac{J_c d}{\left(1+\beta^2\right)L_p^2 B_{ro}} \tag{7}$$

where α is the volume fraction of superconductor and $\beta = B_{tano}/B_{ro}$. The crossover frequency is plotted as a function of temperature in Figure 10 for B_{ro} = 0.5 T and for the 5- and 10-mm twist pitches. Note that the crossover, being proportional to critical current density, decreases with rising temperature. For the longer twist pitch, the crossover is always less than 100 Hz, but for the 5-mm pitch, the crossover is barely in the available frequency range at the lowest temperature.

Consider now the total loss expected in the two-coil test article (to be described more fully in the section "Description of the Coil Tester Rig and the Test Articles"). Noting that the total volume of SC wire in the high-field region is 7.26 cm^3, the volumetric losses in Figure 9 can be converted to the total loss as a function of temperature, twist, and frequency, which is presented in Figure 11.

It is useful to compare the range of expected losses shown in Figure 11 to the estimated tare to be expected in the experiment due to radiation and conduction heating of the coil pack. See Appendix C for more detail. A preliminary estimate of the radiation loading, plus an estimate of eddy current heating in the aluminized plastic film that will cover the test article, is 2 W. This is based on the assumptions that (1) the back iron is at room temperature and (2) the entire coil pack is covered with single-layer aluminized plastic film that is striated into small squares to reduce eddy current heating. The heat loading on the experiment pack, from thermal conduction through the residual gas (mainly nitrogen after purging) in the imperfect vacuum outside the pack, may be as much as 30 W in the hydrodynamic pressure regime (down to roughly 10^{-3} torr), then reducing rapidly to around 100 mW at 10^{-4} torr. Clearly, the latter level of vacuum or better will be required to keep the tare from dominating the measurement.

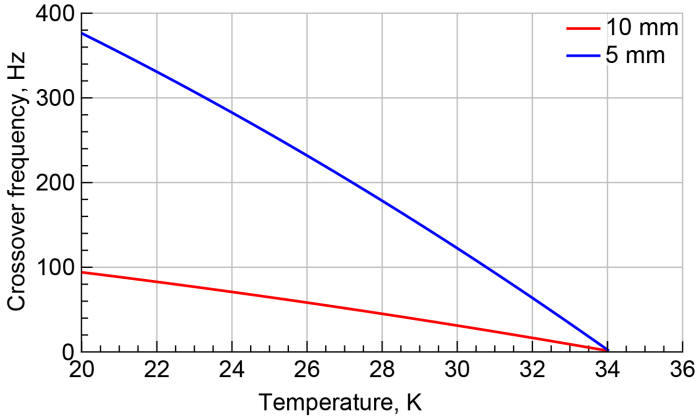

Figure 10.—Frequency at which hysteresis and coupling losses are equal for 31-μm-diameter filaments for β = 0.6, B_{ro} = 0.5 T, and J_c given by Equation (1). Twist pitch = 10 mm (red curve) and 5 mm (blue curve).

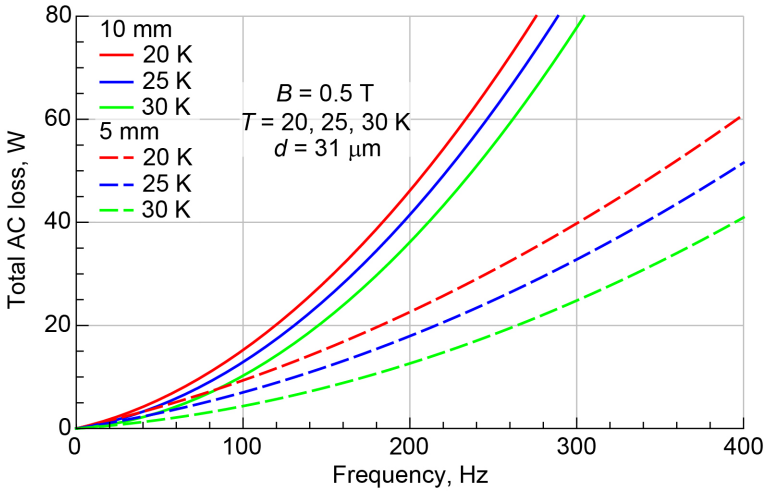

Figure 11.—Loss in two complete coils as function of frequency at three temperatures, 30 K (green), 25 K (blue), and 20 K (red), for two twist pitches, 10 mm (solid curves) and 5 mm (dashed curves), at 0.5 T amplitude, β = 0.6 for SC filaments of 31 μm diameter.

Because the dependence upon frequency is linear for hysteresis loss and quadratic for coupling loss, it is convenient to calculate the loss per cycle, both in the predictions and in the eventual experiment. A plot of the loss per cycle versus frequency has the convenient feature that it is linear and visually separates the two losses. The ordinate intercept of the line is the hysteresis loss per cycle; its slope is the coupling loss per cycle squared. Such plots for three temperatures and two twist pitches are shown in Figure 12(a), on a wire volumetric basis, and in Figure 12(b), for two complete coils. Also shown in Figure 12(b) is an aqua curve that represents the extra heat loading per cycle due to a postulated tare heat leak of 2 W, for comparison. It will be favorable to operate at frequencies where the tare is considerably less than the AC loss to be measured.

Rotor Critical Speeds

Modal analysis and transient analysis have predicted that certain rotor speeds should be avoided or passed through quickly. See Appendix C of Hartwig et al. (2019) for details. The rotor manufacturing specifications call for balancing to 0.1 oz-in. (ISO balance quality grade G 0.16). It is predicted that a rotor acceleration of 5.5 r/s^2 (53 rpm/s) is adequate to pass safely through a critical speed in the 4,200 to 4,300 rpm range. This acceleration rate will be easily achieved by the 18-kW motor. How close to that range it is possible to dwell long enough to do calorimetry will likely be known only after experimental modal analysis is performed on the rotor and actual accelerometer measurements are obtained in the running rig.

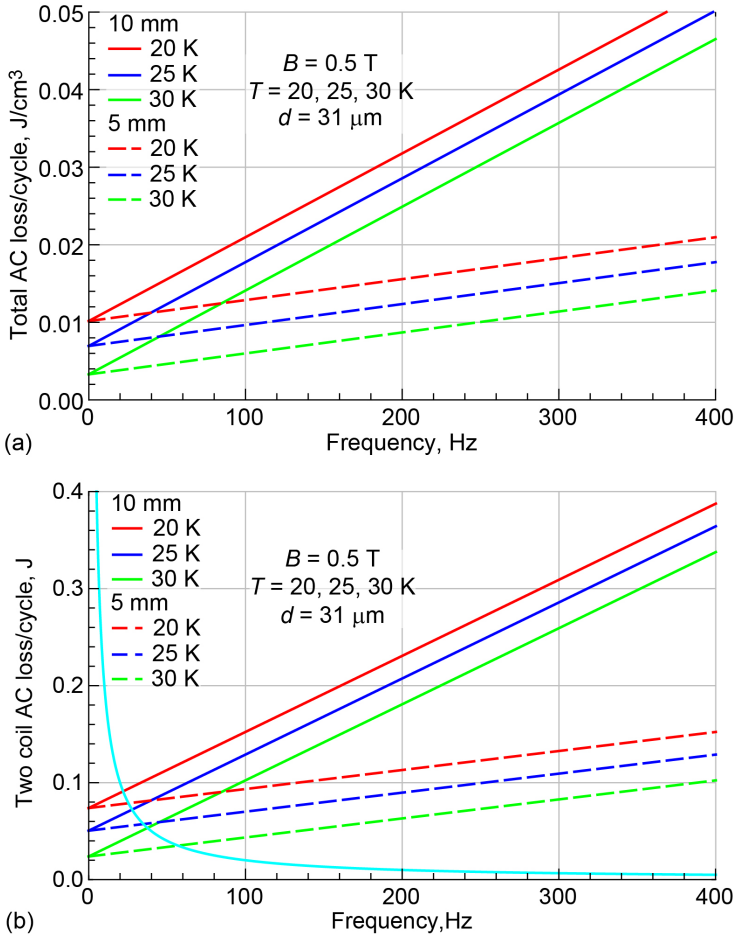

Figure 12.—Loss per cycle. (a) On volumetric basis versus frequency at three temperatures and twist pitches of 10 mm and 5 mm at 0.5 T amplitude and β = 0.6, for SC filaments of 31-μm diameter. (b) For two complete coils versus frequency at three temperatures and twist pitches of 10 mm and 5 mm at 0.5 T amplitude and β = 0.6, for SC filaments of 31-μm diameter. Curve represents extra heat loading per cycle due to postulated tare heat leak of 2 W.

Description of the Coil Tester Rig and the Test Articles

The coil tester rig is modeled after the AFRL SAM (Spin Around Magnet) rig, which is described in several reports (Haugan, 2015 unpublished and Murphy et al., 2013, 2015, 2017). The rotor of that rig was copied exactly. The inner radius of the back iron of the rig was increased to give a larger annular space for creating lower temperatures than were intended in the SAM rig. The SAM rig and the NASA Glenn rig have the advantage of being able to maintain a magnetic field of a strength comparable to that expected in an actual SC stator, even at relatively high frequencies of 400 Hz. AC loss rigs that produce the applied field with arrays of current-carrying coils, like those described by Pamidi et al. (2007 and 2016 unpublished), can control field frequency and strength as well as the field character (oscillating, rotating, or combinations thereof). However, the field strength in such rigs is limited to a maximum that is inversely proportional to frequency.

Cutaway drawings of the rig and an enlarged insert are shown in Figure 13(a) and (b) and a photograph in Figure 13(c). Figure 13(d) shows a cross section through the rig with a test article assembly inserted between the rotor and the back iron.

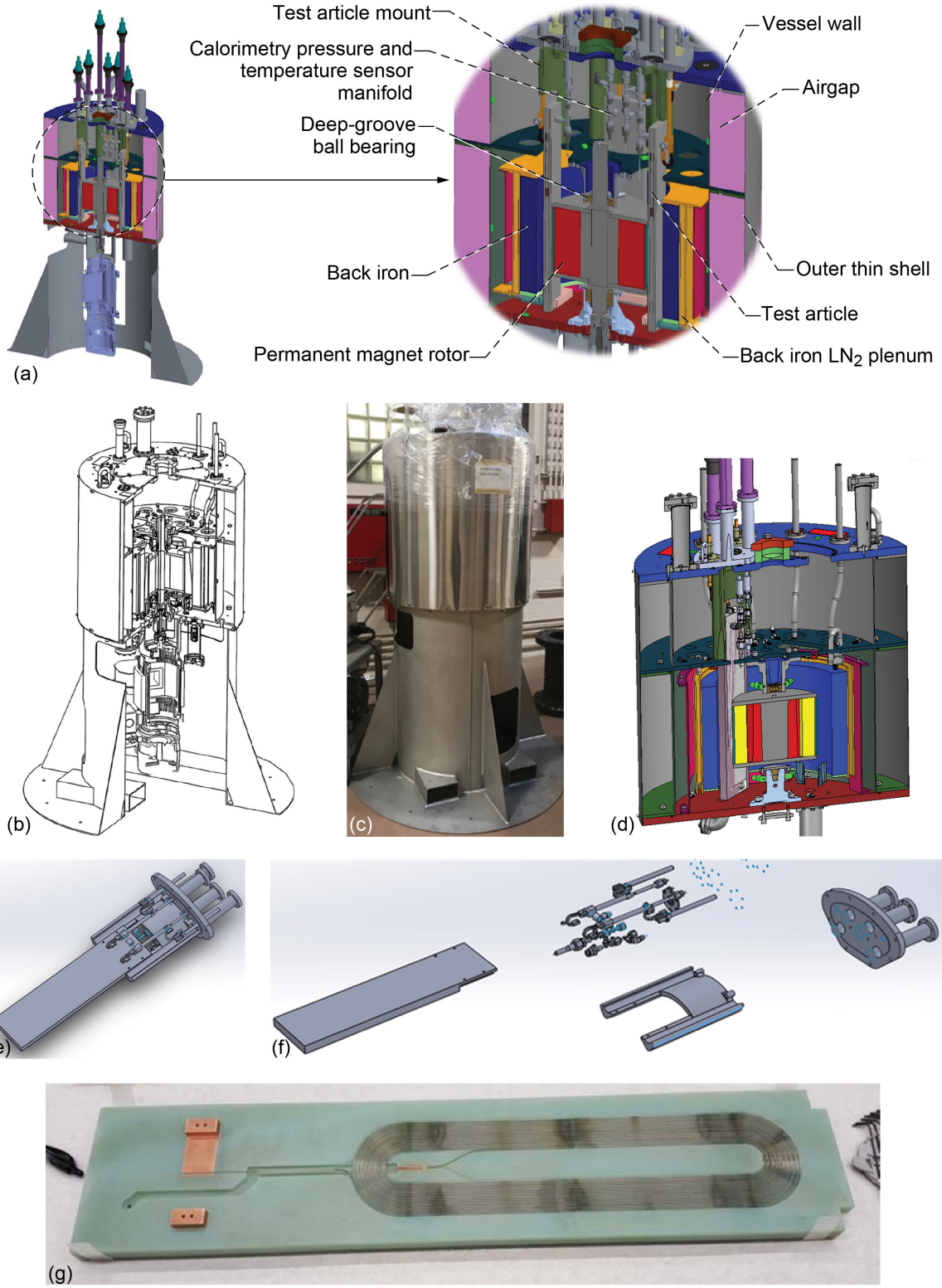

Figure 13.—Coil tester rig. (a) Sectioned views of SC coil tester with major parts labeled. (b) Cutaway drawing of coil tester rig. (c) Photograph of coil tester rig before installation. (d) Cross-sectional drawing of rig with coil pack in place. (e) CAD graphic of test article assembly. (f) Exploded view of test article assembly showing coil pack, fluid flow and current supply components, structural support, and top plate with its cryogenic bayonet fittings. (g) One coil shown on coil former with cover plate removed.

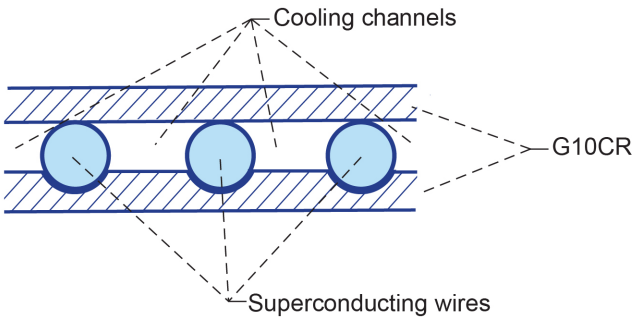

Figure 14.—Cross section through portion of coil showing three of its turns bounded by grooved and ungrooved sheets of G10 bounding turns to form cooling channels.

Figure 13(e) presents a CAD graphic of the test article assembly, which consists of a physical support structure, a sealing flange, bayonet fittings to connect with the fluid flow circuit, and the coil pack. The components are shown in an exploded view in Figure 13(f). The coil pack is formed by three 5-in.-wide layers of glass epoxy laminate (G10 or G10CR) that sandwich two race-track-type coils of SC wire (alternatively, a collection of straight cut wires) and create cooling passages between the wires. One coil is shown on a grooved sheet of G10 in Figure 13(g). The wire selected for the first coil, Strand #3667, is made up of 114 filaments, a Cu10Ni matrix, Cu10Ni central filaments and a Cu30Ni outer sheath; commercial CuNi alloy material was used. The strand was twisted at a 10-mm pitch and sized to 0.85 mm for the coil. Grooves in the G10 on one or both sides of the coil separate the turns to form cooling passages for GHe flow. A cross section through wires and channels in such an arrangement is shown in Figure 14.

Fluid Flow and Heat Transfer Considerations

Figure 15 is a diagram of the GHe flow circuit, showing the arrangement of the components between two vessels, the ICE-Box and the core rig or coil tester. The total required volume flow in the circuit determines the size of the pump or fan required to circulate the coolant in the system. Figure 16 shows the value of that total flow as a function of the fluid velocity in the channels, which is the mathematically independent parameter. The following section shows that a flow velocity in the channels on the order of 8 m/s, with corresponding single-channel mass flow of 0.038 g/s and total mass flow (in 34 channels) of 1.29 g/s, will provide good heat transfer and an acceptable value of the warmup from the fluid inlet to the outlet. It is, however, very near the low end of the flow capability of the fan, and the pressure drops predicted for the flow circuit require a pressure head near the maximum capability of the fan, given the low density of the fluid. The pressure-head versus volume-flow-rate capability of the Böhmwind fan (Stirling Cryogenics) is discussed in Appendix D. Unfortunately, the fluid pressure difference produced by the pump depends on the fluid density, so the maximum fluid pressure difference available depends on both the temperature and the pressure of the He in the fan. The highest pressure difference available would be for 20 K (the lowest considered temperature) and He gas at 6 bar pressure at the pump inlet, which works out to be 0.017 MPa (2.5 psi).

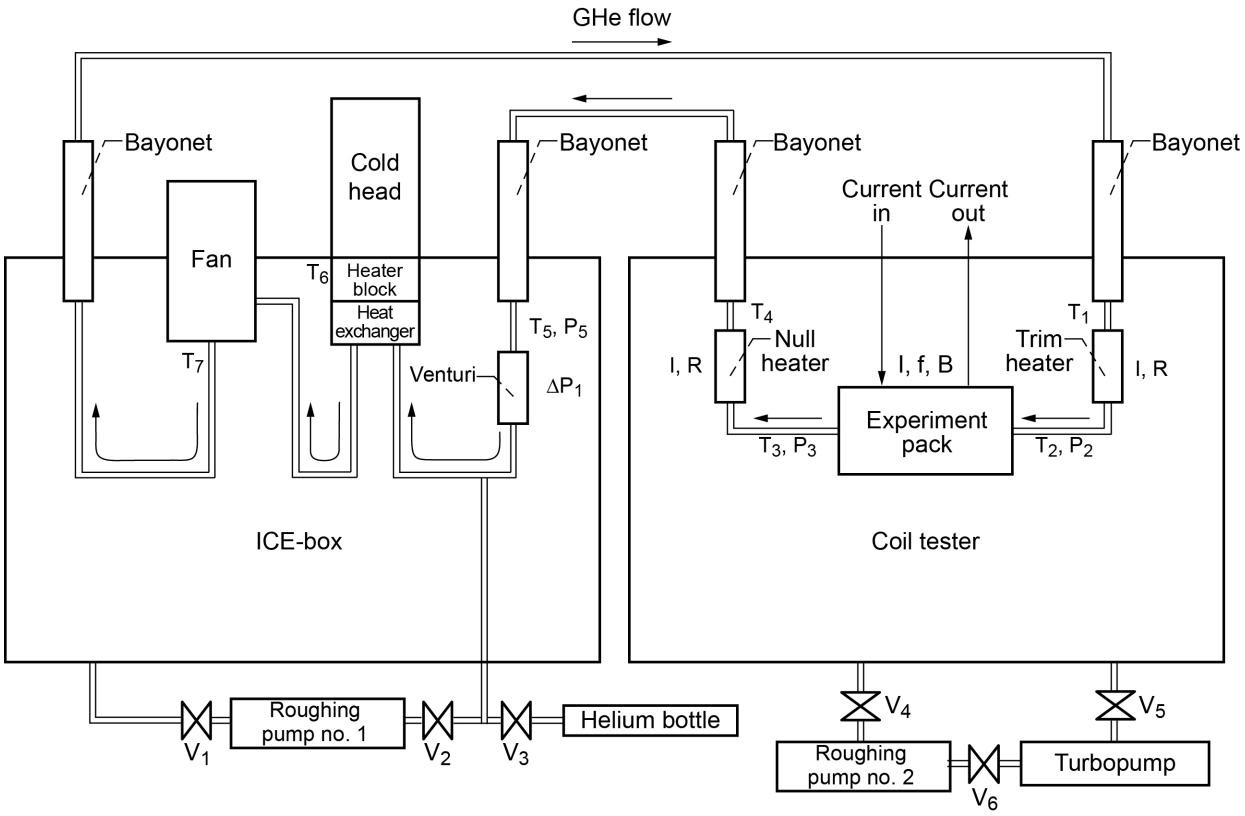

Figure 15.—Diagram of GHe flow circuit, showing arrangement of components between two vessels: ICE-Box and coil tester.

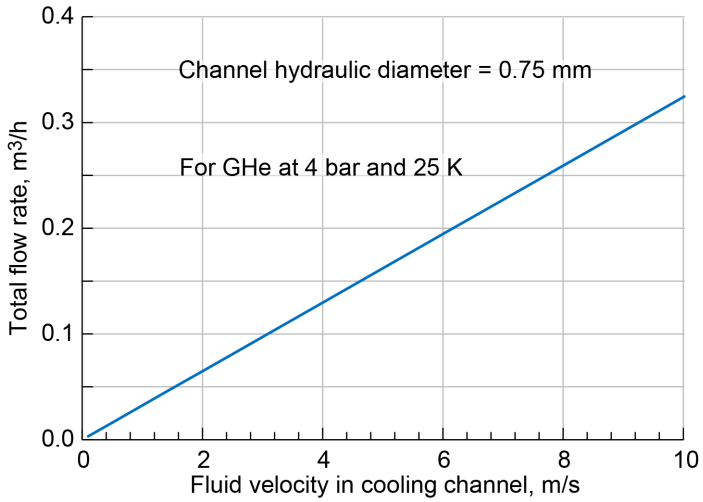

Figure 16.—Total system flow required for 32 parallel channels as function of coolant velocity in channels.

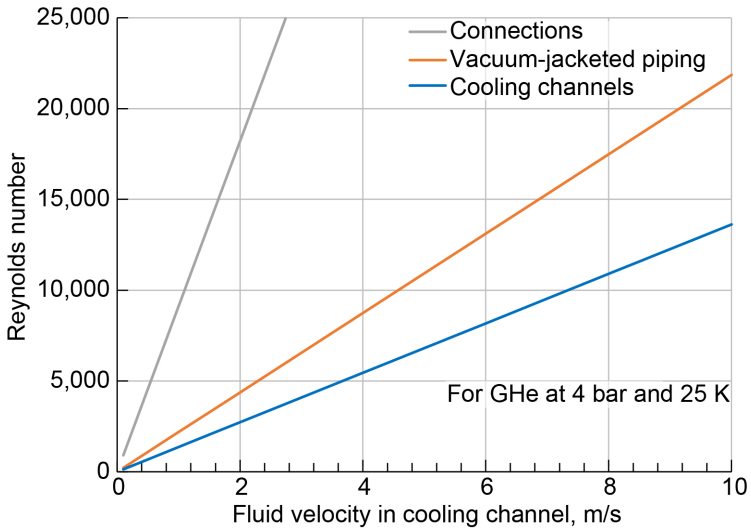

Figure 17.—Reynolds number in three parts of cooling circuit as functions of coolant velocity in channels.

For the bulk of this discussion, the Example Case that was defined in Table 1 is being considered, with an arbitrarily selected flow rate of 8 m/s in the cooling channels. For calculations, velocity in the cooling channels is a convenient independent variable, upon which the pressure drop, all the nondimensional flow parameters (Reynolds number Re, Nusselt number Nu, and Darcy friction factor *ff*), the heat transfer coefficient, and the total warmup depend, as shown from the equations presented in Appendix D and Appendix E. Experimentally, the shaft speed of the fan that drives the helium (He)flow will be controlled, likely with feedback from the mass-flow venturi. Figure 17 shows that the flow in the channels will be turbulent at rates faster than about 2 m/s mass flow.

For the Example Case superconductor (31-μm-diam. filaments with 10-mm twist pitch) and the example fluid loop charging pressure of 4 bar, the results are presented in Table 2, for a channel with fluid flow velocity of 8 m/s with a hydraulic diameter of 0.75 mm, for three superconductor temperatures (20, 25, and 30 K at the axial midpoint), and for two values of filament twist pitch (5 and 10 mm). These results were derived using the fluid flow analysis equations in Appendix D and the heat transfer analysis equations in Appendix E. The equations are applied only at the axial midpoint of the SC sample and assume that the heat transfer rate from superconductor to fluid, the rate of fluid heating per length along the channel, and the pressure drop per length adequately represent the entire length of the experimental sample (not including end turns). The amount of superheat of the wires above the fluid temperature is enough that an iterative solution of the equations was needed to find the fluid temperature. In the first iteration, the fluid temperature was taken to be the same as that of the superconductor. The convergence is rapid, and three or four iterations are sufficient to reduce convergence error to less than 0.1 percent.

Many points from Table 2 are worth noting. For this section on flow, note that the chosen flow rate requires at most 66 m of head for the tabulated conditions. The commercially purchased pump produces about 120 m of head, which could drive higher gas flow rates for improved heat transfer and less warmup in the experiment pack if desired.

TABLE 2.—MAJOR OUTPUTS FROM FLUID FLOW AND HEAT TRANSFER ITERATIVE CALCULATIONS FOR THREE SUPERCONDUCTOR MIDPOINT TEMPERATURES AND TWO TWIST PITCHES*

Filament twist pitch, mm	10	10	10	5	5	5
Midpoint superconductor temperature, K	20	25	30	20	25	30
Midpoint fluid temperature (derived), K	18.6	23.5	28.5	19.3	24.4	29.48
Superconductor hysteresis loss, W/cm^3	2.03	1.39	0.658	2.03	1.39	0.658
Superconductor coupling loss, W/cm^3	4.32	4.32	4.32	1.08	1.08	1.08
Superconductor total AC loss, W/cm^3	6.36	5.71	4.98	3.11	2.47	1.74
Helium density, kg/m^3	10.4	8.17	6.71	10.0	7.89	6.49
Re number in cooling channels	17,600	12,000	8,800	16,600	11,400	8,350
Re number in vacuum-jacketed (VJ) piping	30,100	20,500	15,000	28,300	19,400	14200
Re number in coil tester connections	123,000	92,600	72,300	123,000	92,600	72,300
Total volume flow (34 channels), cm^3/s	153	153	153	153	153	153
Total volume flow (34 channels), m^3/hr	0.551	0.551	0.551	0.551	0.551	0.551
Total mass flow (34 channels), g/s	1.60	1.25	0.98	1.48	1.18	0.98
Inlet-to-outlet warmup, K	5.33	6.22	6.66	2.72	2.79	2.41
Offset from mean fluid temperature, K	±2.66	±3.11	±3.33	±1.36	±1.39	±1.20
Inlet-to-outlet warmup with 2 W tare, K	5.56	6.52	7.03	2.96	3.10	2.79
Heat absorbed by fluid (1 channel), W	1.36	1.22	1.06	0.665	0.528	0.372
Heat absorbed by fluid (34 channels), W	46.2	41.5	36.2	22.6	17.9	12.6
Heat transfer coefficient, W/cm^2-K	0.176	0.148	0.128	0.171	0.144	0.126
Superheat of SC above fluid, K	1.37	1.47	1.47	0.688	0.650	0.524
Pressure drop, two coils in series, Pa	4,883	4,209	3,737	4,771	4,121	3,663
Pressure drop, two coils in series, psi	0.708	0.610	0.542	0.692	0.598	0.531
Head loss, two coils in series, m	47.7	52.5	56.8	48.4	53.2	57.5
Pressure drop, VJ piping, Pa	11.36	9.80	8.70	11.1	9.59	8.53
Head drop through VJ piping, m	0.111	0.122	0.132	0.113	0.124	0.134
Pressure drop in connections, Pa	734	632	562	717	619	550
Head drop through connections, m	7.2	7.9	8.5	7.3	8.0	8.6
Pressure drop entire circuit (except HX), Pa	5,628	4,277	3,798	4,849	4,188	3,732
Total pressure drop (except HX), psi	0.82	0.70	0.62	0.80	0.69	0.61
Total head drop (except HX), m	55	61	65	56	61	66
Required fluid inlet temperature, K	15.9	20.4	25.2	17.9	24.0	28.3

*For all cases in this table, B = 0.5 T, d = 31 μm, P = 4 bar, f = 200 Hz, and fluid velocity in cooling channels is 8 m/s. Losses are based on an iterative procedure that finds the midpoint fluid temperature that, with the iteratively found superheat, yields the tabulated midpoint superconductor temperatures. The head drop values do not include head drop in the heat exchanger (HX) that rejects the heat to the cold head. See Appendix F for more information on the heat exchanger.

Calorimetry and Heat Balance Considerations

It is necessary to resort to some type of calorimetric method to measure the AC losses, because an electrical measurement is not possible. The transport current portion of the AC loss (which is expected to be small enough to be ignored) could, in principle, be measured electrically. But the source of the power that

causes all other losses is the drive system of the PM motor, which produces no potential difference across a sample. Identifying the AC loss portion of the existing drive system power is not considered feasible.

To make the calorimetric measurements, the method used will employ the closed-path GHe circuit in which the fluid is cooled, its flow is regulated, and in which various temperatures are measured. The flow circuit is diagrammed in Figure 15. The flow is forced by a commercially available cryogenic impeller (the Böhmwind fan) that can provide up to 120 m of head. The circulating gas is cooled by an AL325 cryocooler (Cryomech Inc.) that has a published capacity (lift) of 110 W at 25 K and 140 W at 30 K. Flow will be measured by using a venturi, in preference to an orifice, to minimize pressure drop. The cryocooler, a heat exchanger attachment, the fan, the venturi, and provisions for charging the system with GHe are installed in an evacuated, room-temperature vessel called the ICE-Box (Hartwig et al., 2019). Components that are external to that vessel measure, control, and relieve the charging pressure as required. Vacuum-jacketed lines connect the components in the ICE-Box to the experiment in the coil tester vessel, described in a previous section.

In the standard method of calorimetry, the mass flow and the temperatures at the inlet and outlet of the experiment are measured. Then, using the known heat capacity of the fluid, the amount of heat absorbed can be calculated. The system is usually calibrated by using it to measure the heat produced in a known resistor. If desired, that standard approach can be used in these experiments. But it may be possible to obtain data more rapidly by using a modified approach that essentially trades off heat produced in the experiment against the heat added by the known resistor.

In typical calorimetry, if the amount of heat dissipated in the experiment pack changes from one data point to another, a considerable amount of time may be required for a steady state to develop under the new conditions. This settling time can be on the order of a half-hour or more. It is slow because all the components in the entire flow circuit (and even the cryocooler) must relax to new temperatures since the heat coming into the system has changed. In addition to lengthening the time required to perform the experiment, it would increase the keep-out zone around the rotor critical speeds because of concern related to bearing wear.

The time to achieve a new steady-state condition can be minimized by employing a null method of calorimetry. By referring to Figure 18, one can see that if the temperatures T_2 and T_4 are controlled to be constant by feedback control of the heat introduced by the null heater, then the heat from the experiment pack and the heat in the null heater can be traded off against one another without affecting the external circuit at all. The time to approach a steady state sufficient for a good measurement then depends only on the masses and heat capacities of the components between T_2 and T_4, rather than on the entire system. The following steps outline the procedure:

(1) Estimate the maximum power dissipation P_{max} expected in a series of experimental conditions (e.g., at several frequencies of the applied field).
(2) With the PM rotor motionless and without current in the superconductor, supply current to the null heater to produce P_{max} resistive heat.
(3) Using a rough setting of the coarse heater mounted on the cryocooler cold head and finer feedback control of the trim heater (between T_1 and T_2), control the temperature T_2 to be a desired constant value.
(4) After the system reaches a steady state, close a second control loop on the temperature T_4, using the null heater as the effector.
(5) Raise the field frequency to a desired value and observe the settling time of temperature T_3. That time should be relatively short compared to the settling time in step 4. The observed decrease of power into the null resistor is then equal to the power added to the experiment pack.

The only issue that arises here is that the mass flow rate must not change over the course of the series of experiments during which the tradeoffs are being made between experiment pack power and null resistor

power. A closed loop on the venturi signal with the fan speed as the effector should keep that rate constant if it has any tendency to change. The level of uncertainty might actually be lower in this null method than in the standard approach because it is unnecessary to know the actual fluid flow rate for the null case—only that it does not change. Accurate calibration of the flow venturi is not required at all, only good sensitivity.

It may be noted that the tare heat leak into the experiment pack can be found in two ways. One is simply by the standard calorimetry method using temperatures T_2 and T_3. The other is by observing T_1 and T_3 and using standard calorimetry to obtain the measured heat versus the heat supplied by the trim resistor. The tare is then the negative of the abscissa intercept of the measured power plotted versus the power supplied to the trim resistor.

Discussion of the Results

The main questions prompting this study were whether He gas at reasonable pressure had enough heat capacity and could give a high enough heat transfer coefficient to limit the superheat and the total warmup from input to output to acceptable values. These questions become even more problematic when dealing with higher loss samples. Results of representative iterative solutions for warmup and superheat are presented in Table 2 and in Figure 19 for the He pressure of 4 bar, frequency of 200 Hz, and cooling channel flow velocity of 8 m/s. These values of pressure and flow are not the maximum possible in the system, but rather are deemed representative without stressing the equipment.

The predicted values for superheat (ranging from about 0.5 to 1.5 K) do not raise much concern, but they show that to suppose that the superconductor and fluid temperatures are the same would be a poor approximation. The inlet-to-outlet warmup (between roughly 2.5 and 6.5 K) does raise concern because of nonuniformity of the sample temperature. These points are further discussed in the following subsections. However, at this point note that mitigation of these concerns is possible. Nearly all the calculated results presented in this report are for He pressure of 4 bar and flow velocity in the cooling channels of 8 m/s, which may be considered nominal values somewhat lower than system design maximum values. A pressure of 6 bar and a fluid velocity of 12 m/s are considered possible; for those values, both warmup and superheat are reduced. Results for those conditions are shown in Figure 20. Both warmup and superheat are roughly half those of the values shown in Figure 19.

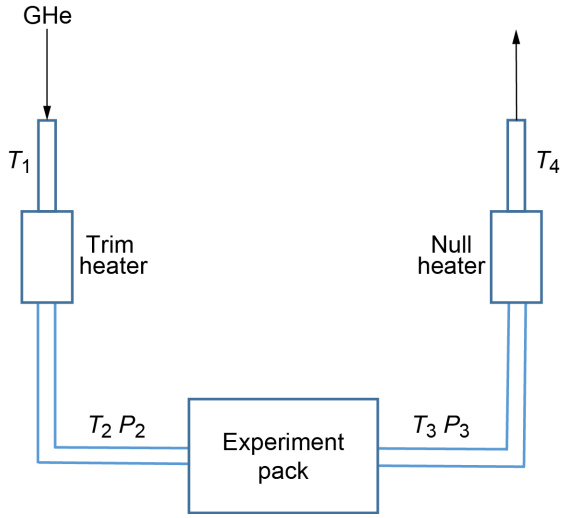

Figure 18.—Null method for calorimetry.

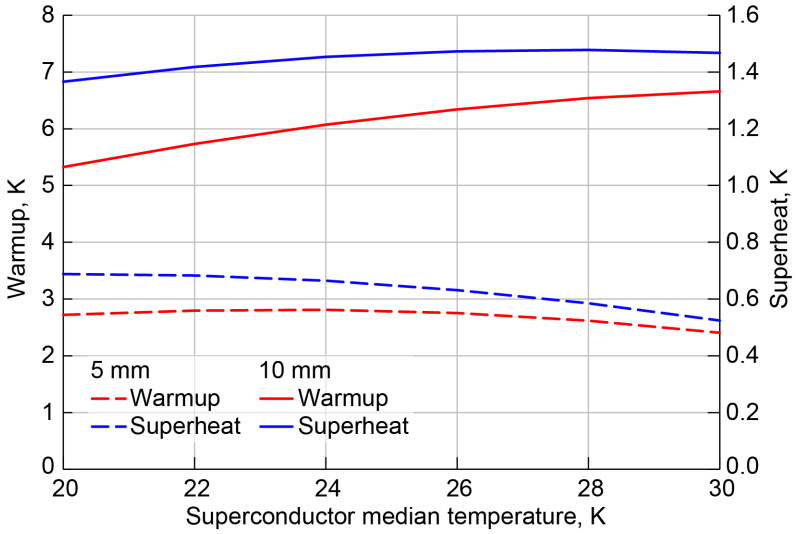

Figure 19.—Warmup (red curves and left scale) and superheat (blue curves and right scale) as functions of superconductor midpoint temperature for twist pitches of 10 mm (solid curves) and 5 mm (dashed curves). He pressure is 4 bar, frequency of 200 Hz, and velocity in cooling channels is 8 m/s. Calculated values do not include any tare heating.

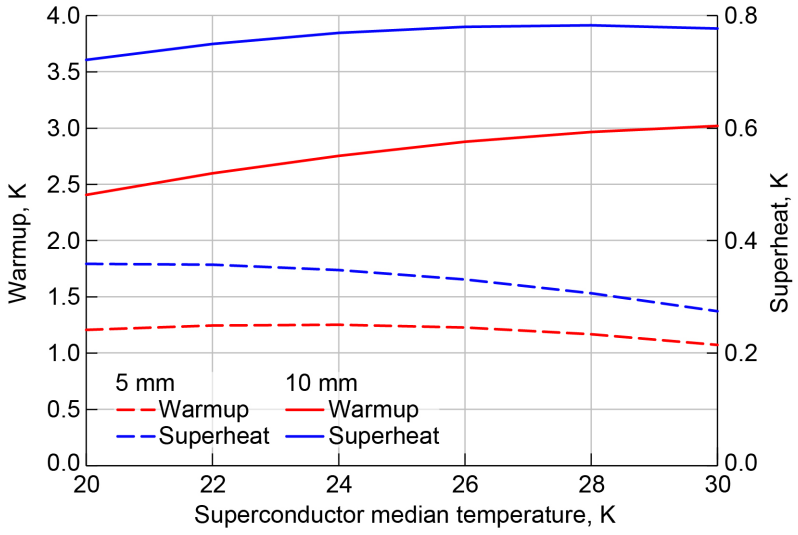

Figure 20.—Warmup (red curves and left scale) and superheat (blue curves and right scale) as functions of superconductor midpoint temperature for twist pitches of 10 mm (solid curves) and 5 mm (dashed curves) for 6 bar He pressure, frequency of 200 Hz, and 12 m/s velocity in cooling channels. Comparison with Figure 19 shows that both warmup and superheat are significantly reduced. Calculated values do not include any tare heating.

Temperature Dependence of Losses

First, note from Table 2 that both the AC losses and the density of GHe decrease as temperature increases. The decrease in AC loss stems from the decrease of critical current density with temperature. Because the AC loss and the gas density do not change at the same rate, some derived quantities are monotonic in temperature and others are not. Some quantities depend only on He properties, others only on SC properties, and some on both.

Note that the coupling loss is not a function of temperature (because the constituents of the matrix are all in their residual resistivity range of temperature), but it does depend on the square of the twist pitch. The hysteresis loss, which is proportional to critical current density, falls rapidly with temperature, as shown in Figure 3. For the 5-mm twist pitch, the hysteresis loss is about twice the coupling loss at 20 K, but at 30 K, it is only about 70 percent as much. It may be possible to approximately measure the coupling loss above the superconductor's critical temperature T_c because the pure Nb sheaths around the SC filaments will have low resistivity compared to the other components of the matrix and may carry coupling currents almost as large as the superconductor would below T_c.

Superheat

As noted previously, the temperature of the superconductor cannot be directly measured in the experiments, but it can be estimated from the cooling model (see Appendix D and Appendix E). The predicted values of superheat range from around 0.5 to 1.5 K for 4 bar pressure and 8 m/s flow velocity. At maximum pressure and flow, the range is reduced to between 0.3 and 0.8 K. These superheat values can be reasonably well predicted and used together with measured fluid temperatures to calculate the superconductor temperature. For higher loss samples, it is necessary to depend more heavily on the heat transfer model.

Another way in which superheat of several degrees has an effect is that the lowest available temperature for the superconductor may be impacted. With high superheat, the He exiting the experiment is several degrees cooler than the wire, the cold head must be cooler than the fluid, and the lift available at the required cold-head temperature may be lower than the sum of all the heat inputs to the flow loop. Nevertheless, the values of superheat that are predicted do not appear to represent serious limitations on the experiments.

Warmup

This issue might appear to be more serious than superheat. The 6.2 K warming of the fluid from the inlet to the outlet (for the example condition of T = 25 K, B = 0.5 T, pressure = 4 bar, f = 200 Hz, GHe velocity = 8 m/s, d = 31 μm, and twist pitch = 10 mm) raises concern because the superconductor at the outlet is substantially warmer (6.2 K) than at the inlet. The superconductor's critical current density would therefore be much lower at the outlet, so the hysteresis loss would be much lower. This appears to be a poorly defined experimental condition. However, Figure 21 shows that the AC loss of the superconductor as a function of temperature is not far from linear, so using a midpoint temperature to represent the entire wire should be reasonably good. Furthermore, for high loss conditions, the temperature increase can be cut in half simply by populating only one side of the experiment pack with superconductor. To reduce the warmup even further for high loss cases, fewer turns can be used in coils and shorter samples can be used in the case of straight, short-sample wires.

In most cases, it may not be necessary to have data up to 200 Hz to define the two loss components. The slope and intercept of the curves in Figure 12(a) (or the equivalent second-order polynomial fit) must be determined. which likely requires frequencies only up to approximately 100 Hz.

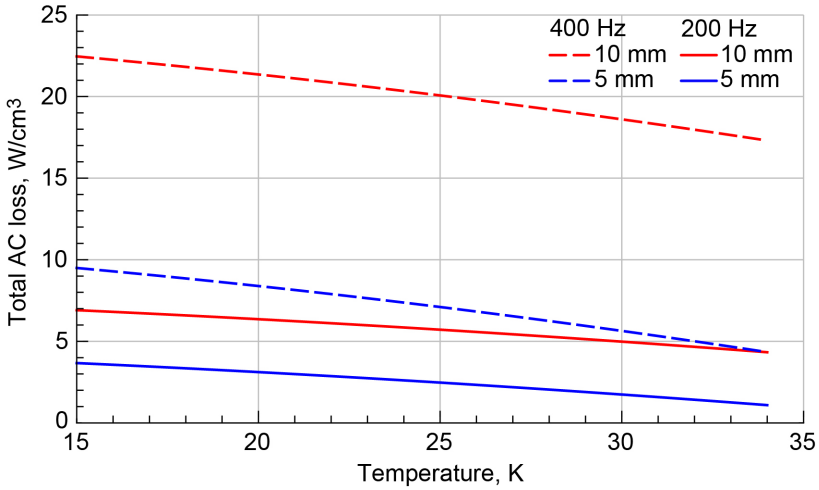

Figure 21.—Dependence of total loss on temperature for 200 Hz (solid) and 400 Hz (dashed) for twist pitches of 10 mm (red) and 5 mm (blue), showing near linearity of loss versus temperature.

The representative results for the 10-mm twist pitch presented in Table 2 and Figure 19 reflect the high side of the losses that the team hopes to measure in the coil tester because they are based on filament size and twist pitch that are currently available together in wires of about 0.85 mm in diameter. Lower loss wires that combine the smallest filaments and the tightest pitch together will likely appear in the future. Lower loss samples are already available as cables of similar outer diameter, but these have much smaller filament diameters inside each strand of the cable. Estimates of losses in cables are not included in this report. The warmup due to tare heat inputs is not included in the graphs. The tare heat input is expected to be much less than 2 W. See Appendix C for additional discussion.

Overall, the team has concluded that warmup will not be a serious issue in the experiments.

Field Variation Over Sample Volume

The considerable variation of field with position in the annular space available for the experiment has been noted above. Both the radial and axial dependence of the field will need to be accounted for when comparing results with predictions. For complete coils, an integration over axial position, as well as treating the two sides of the existing coil former separately, will be necessary. For short enough samples, mounted on only one side of the coil former, the variation of the field strength can likely be neglected. The field in the region of the end turns is reduced but, not being zero, contributes to loss. This contribution to loss will complicate the postanalysis of experiments, but it cannot be avoided.

Limits on Accessible Frequencies Versus Sample Temperature

The highest feasible frequency for which the cryocooler can remove the heat produced from AC losses plus all other sources of heat in the closed circuit depends on several factors. These include the cryocooler lift capacity versus temperature, the superconductor losses, the superconductor temperature, heat leaks into the system, fan work, fan inefficiency, and the cold head's heat exchanger characteristics. Some of these cannot be evaluated accurately until measurements on the flow system can be carried out. But with assumptions for the missing data, the frequency higher than which the cryocooler cannot remove the losses and other heat is plotted in Figure 22 as a function of the superconductor temperature at its axial midplane. Figure 22 also shows the frequencies at which the hysteresis and coupling losses are equal

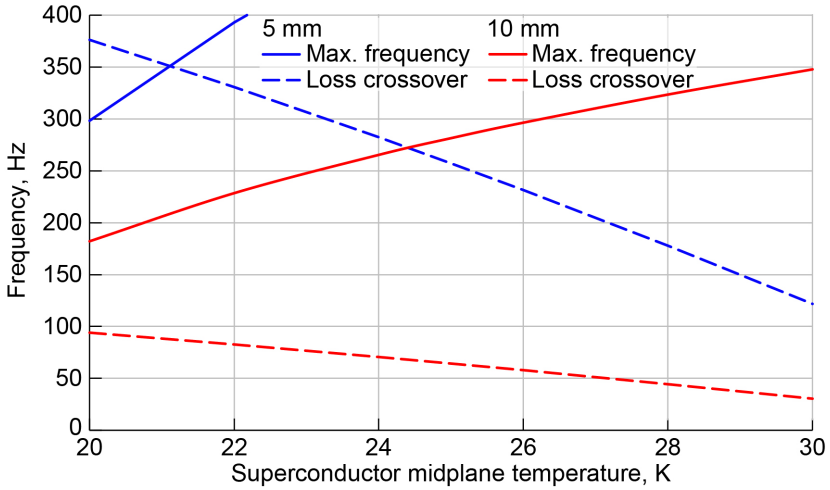

Figure 22.—Highest frequency for which losses can be removed by the cryocooler (solid) and crossover frequency (dashed) versus superconductor temperature at midplane. Twist pitches are 10 mm (red) and 5 mm (blue); filament size is 31 μm. The assumed temperature difference between cold head and He stream at exit of heat exchanger is 2 K. Pressure is 4 bar and coolant velocity is 8 m/s.

(the crossover frequency). Separating the hysteresis and coupling losses is easier if data well above the crossover frequency are available. This is seen to be reasonably well satisfied for the entire 20 to 30 K range for the samples with 10-mm twist pitch (red curves), but possibly not lower than 23 K or so for the 5-mm twist pitch (blue curves).

Experiment Sensitivity for Lower Loss Samples and Conditions

In general, the lower the loss under any experimental condition, the more uniform the superconductor temperature will be and the lower the superheat will be. However, the accuracy will ultimately suffer as the inlet-to-outlet temperature span falls because of temperature sensor sensitivity and uncertainties. Lower loss is expected for wire samples with smaller filament diameter, tighter twist, and higher matrix resistivity and for higher temperatures and lower frequencies. However, the sensors to be used for this purpose are calibrated Cernox® (Lake Shore Cryotronics, Inc.) sensors, which have a stated uncertainty of less than 10 mK. Therefore, the difference between inlet and outlet temperatures can be as small as 0.4 K (in excess of the tare warmup) before the possible uncertainty reaches 5 percent. The temperature span can easily be increased by lowering the pressure or the flow rate of the He in the system, at the expense of a higher superheat value.

Other Sources of Uncertainty

Several factors have been identified that introduce uncertainty into the measured results. These include the elliptical character of the magnetic field, variations of its strength over the axial and radial extent of the SC sample, the axial field component on end turns of coils, uncertainties in the actual superconductor temperature (which must be deduced from modeled superheat and from inlet and outlet He temperatures) and uncertainties in the calorimetric measurements. It was noted that accurate flow measurement is not necessary in the null method of calorimetry that is to be used; it is only required that the flow be held fixed within acceptable bounds.

Head Loss and Heat Rejection Capacity of the Cold Head Heat Exchanger

The heat exchanger mounted on the cold head has been ignored up to this point. Its head loss should be expected to be small and the heat transfer good by design. However, the published characteristic of the exchanger supposes that the operating pressure is 20 bar, which is much higher than the experimental setup can initially tolerate. The consequences of this are not easy to evaluate, but Appendix F develops some analysis and predictions that indicate that the intended operating pressures should be sufficient.

Concluding Remarks

The overall assessment of this work is that helium gas will be a satisfactory calorimetric fluid for measuring alternating current (AC) losses in magnesium diboride (MgB_2) short samples and coils. The experiment's sensitivity will be adequate because experimental conductor packs with multiple parallel paths for fluid flow will be able to accommodate sufficient volume of conductor to yield easily observable losses that exceed the expected tare heat leak. As is often the case in superconductor experiments, it will not be possible to measure the conductor temperature directly. However, measurements of fluid inlet and outlet temperatures and the use of a model to predict the superheat of the sample higher than the local fluid temperature should be adequate to correlate the loss data with the local sample temperature. The amount of heating from inlet to outlet of the experiment can be limited to a few degrees by choosing the total sample size. The variation of field strength with position will be greater in the rig built at NASA Glenn than in the Air Force Research Laboratory (AFRL) rig because of the expanded annular gap between rotor and back iron that was required to accommodate the lower operating temperatures and the provision for future experiments on larger and more realistic motor coils. Consequently, short straight samples will give the best AC loss data for correlation with models. Correlating loss data in coils will require integrating the losses over a range of magnetic fields and temperatures.

Appendix A.—Comparison Between Old and New J_c Fits

The two analytical expressions for filament critical current density J_c to be compared are the older one:

$$J_c^{\text{filaments}} = 8.49 * \left[\left(1.907\ T^2 - 121.5\ T + 2027.9\right) - \left(1.0268\ T^2 - 64.414\ T + 1116\right) * Ln(B) \right] \quad \text{(A.1)}$$

which was used in Brown et al. (2020) and prior publications, and the new one:

$$J_c^{\text{filaments}} = \left(-4.4 + 1.6 * B\right) * T^2 - \left(60.4 + 73.6 * B\right) * T + \left(7966 - 966 * B\right) \quad \text{(A.2)}$$

where T is temperature and B is magnetic field strength.

The older formula was not originally intended to fit data at field strengths less than about 2 T and was not for temperatures higher than 28 K. The new fit was produced to improve the match to experimental data for the low field region at and less than 1 T and at temperatures from 20 K to somewhat higher than 30 K. The data comes from Figure 9 of Hyper Tech (2013 unpublished). The new fit is linear in magnetic field and quadratic in temperature. It fits the sparse experimental data exactly for $B = 0$ and $B = 1$ for T = 20, 25, 30, and 35 K. Figure A.1 shows the comparison at three values of magnetic field strength. Note the unphysical trend at temperatures higher than 28 K of the older fit, whereas the new fit exhibits a field-dependent critical temperature that varies from about 31.5 K at 1 T to 36 K for zero applied field.

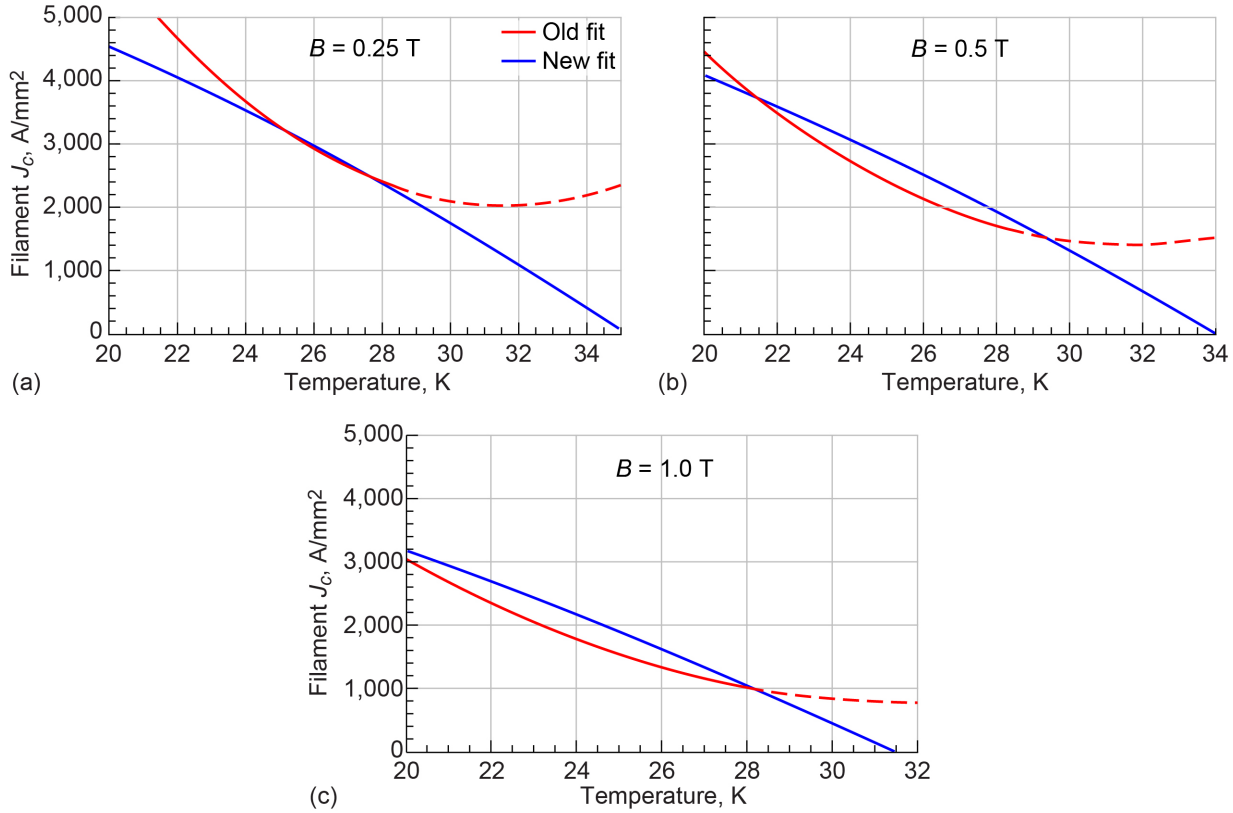

Figure A.1.—Comparison of critical current densities for three values of applied magnetic field for old fit and new fit. Old fit was not intended to be used at temperatures higher than 28 K, but its values are shown as dashed lines higher than 28 K for comparison. (a) B=0.25 T. (b) B=0.5 T. (c) B=1.0 T.

Appendix B.—Full Penetration Field for Superconducting Filaments

Here it is shown that the penetration field for the filament size that will be used is much lower than 0.4 T. The full penetration field is given by Carr (2001), page 83, Equation 7.27:

$$B_p = \frac{\mu_o}{\pi} d J_c \tag{B.1}$$

where d is the diameter of the filaments and μ_o is the permeability of free space.

A plot of the penetration field as a function of the filament diameter and the filament J_c is shown in Figure 4. For the lowest expected temperature of 20 K, for which the critical current density and penetration field will be highest, the filament J_c is at most 5,000 A/mm^2, which, from Figure B.1, yields a penetration field of 0.06 T for 31 μm filaments. From Figure 7, the field amplitude between the magnet endplanes is always > 0.23 T, which is nearly 4 times as high, which justifies the use of only the full-penetration formulas in that region. In the region of the end turns of coils, the radial field becomes weaker, but the axial field becomes significant, maintaining the total transverse field on the filaments higher than the penetration field. For smaller diameter strands, full penetration is even more easily assured.

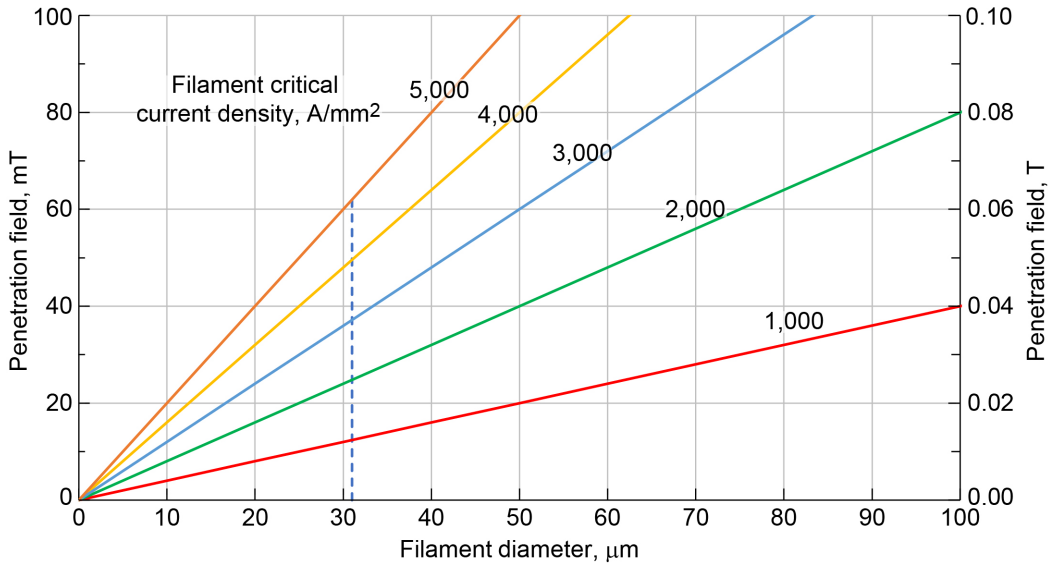

Figure B.1.—Full penetration field for SC filament as function of its diameter and filament critical current density. Maximum filament diameter anticipated in testing (31 μm) is indicated by dashed vertical line.

Appendix C.—Estimating the Tare Heat Leaks Into the Experiment Pack

Three contributions to the tare heat input are considered: thermal conduction through the residual gas in the vessel, radiation from surfaces that have a view factor from the test article, and eddy current heating of the aluminized plastic film.

C.1 Gas Thermal Conduction

The heat load on the experiment pack due to gas conduction can be estimated as a function of the gas pressure in the vacuum space. There are two different regimes: the hydrodynamic regime near atmospheric pressure where gas molecules collide with one another and the free-molecular regime at low pressure where gas molecules may travel from cold to hot walls without any collisions. In the hydrodynamic regime, the gas heat conduction between two plates of area A, separation d, and temperature difference of ΔT is

$$Q_{dot} = \lambda A \frac{\Delta T}{d} \tag{C.1}$$

where λ is the mean value of the gas thermal conductivity between the two plates. This hydrodynamic contribution is constant at high pressure but drops to zero below the transition point between the hydrodynamic and the free-molecular regimes. This transition occurs when the mean free path, $\bar{l}$, is equal to the distance between hot and cold surfaces. Assuming that the gas is molecular nitrogen, then the mean free path $\bar{l}$ is given by

$$\bar{l} \cdot P = 4.4 \times 10^{-3} \frac{T}{273} \text{cm} \cdot \text{torr} \tag{C.2}$$

Assuming an average gas temperature of 150 K, the result obtained is

$$\bar{l} = \frac{2.4 \times 10^{-3}}{P} \text{cm} \tag{C.3}$$

To simplify the geometry, one can divide the surface of the coil pack into several zones that are approximately the same distance from a hot surface, for instance, d = 0.4, 1, and 2 cm. Then the pressure at which $\bar{l} = d$ and the hydrodynamic regime heat flow contribution can be calculated for each zone. Only the region near the coils need be considered because the G10 has low enough thermal conductivity to sustain large temperature gradients. Summing the contributions of zones together results in the total hydrodynamic heat flow.

In the low-pressure, free-molecular regime, the heat conduction is independent of separation and varies linearly with pressure according to the equation

$$Q_{dot} = k a_o P A_i \Delta T \quad \text{[Watts]} \tag{C.4}$$

The k is a constant with a value of 1.2 for air, A_i is the area of the coil pack in meters squared, P is in Pascals and a_0 is a dimensionless number between 0.3 and 1.0. It is related to the accommodation coefficients of the relevant surfaces, which depend upon geometry, surface condition, type of gas, and temperature. For this estimate, assume a_0 = 0.4. The plot in Figure C.1 shows the resulting sum of the heat from the

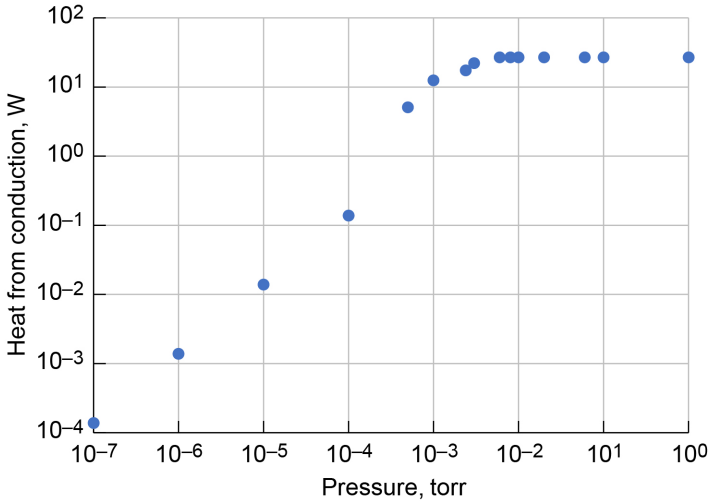

Figure C.1.—Gas conduction heating of experiment pack as function of residual gas pressure in vessel. Gas is approximated as pure nitrogen.

hydrodynamic regime and the heat from the free-molecular regime. It is seen that between roughly 10^{-3} and 10^{-4} torr there is a marked change in conduction as the mode of transfer changes from that of the hydrodynamic range to that of free-molecular flow. It is important to ensure the vessel can be pumped to 10^{-4} torr or lower. At 10^{-4} torr, the conduction load would be on the order of 0.1 W and drops rapidly at lower pressure.

C.2 Radiation

The radiation loading is estimated, assuming all surfaces that can radiate to the test article are at 300 K. The rotor surface is assumed to have an emissivity of 0.09. All other radiators are assumed to be covered with, or at least shielded by, the type of aluminized film that is used on the test article and to have emissivity of 0.035. The radiation loading P_{rad} of each section of the experiment pack with area A and emissivity ε_{TA} is then estimated as

$$P_{rad} = P_o * \varepsilon * \varepsilon_{TA} * A \tag{C.5}$$

where the radiating surface emissivity ε is 0.09 for the surface of the rotor and 0.035 for all other areas, and P_o is approximated as 460 W/m^2. For an experiment pack 0.5 m long, 0.025 m thick, with 0.2 m of the length facing the rotor, the radiation received by the rotor-facing portion (including the edges) is 0.081 W and the amount received by the rest of the experiment pack is 0.049 W for a total of only 0.13 W.

C.3 Eddy Current Loss in Radiation Shielding

The entire experiment pack will be covered by single-side-aluminized plastic film with the aluminum layer striated into 1-cm squares. The aluminized layer is 56 nm thick and has a room-temperature (RT) resistance of 8 Ω/square, which corresponds to a resistivity of 4.5 μΩ-cm. Bulk aluminum resistivity at RT is 2.7 μΩ-cm. The RT excess, 1.8 μΩ-cm, of the aluminized layer resistivity over bulk resistivity is due to some combination of surface scattering, impurities, and defects, and it is presumed to persist unchanged down to 30 K and lower, where the temperature component of resistivity is negligible.

To estimate the eddy current heating due to an applied sinusoidal field perpendicular to a thin square region of aluminum, consider instead the easily calculable loss in a circular region. Presume that the losses in circles inscribed in and circumscribed around the square will bracket the actual loss in the square. The approach is to calculate heating in an annulus dr at radius r due to $B = B_o \sin(\omega t)$, then to integrate the loss from zero to the radius a of the circle.

The electromotive force inducing current in the annulus is $\pi r^2 B_o \omega \cos(\omega t)$. The resistance R of the annulus is $R = \rho 2\pi r/(t dr)$, where t is the thickness of the aluminum and ρ is its resistivity. The amplitude of the resulting power dissipated in the annulus is $\pi^2 r^4 B_o^2 \omega^2 t\, dr/(2\pi\rho r)$. Integrating this expression over r from zero to the circle radius r_c gives the amplitude of the power dissipated in the circular region $[\pi t B_o^2 \omega^2/(2\rho)]\int r^3 dr$. Noting that r_c will be $a/2$ for an inscribed circle and $a/\sqrt{2}$ for a circumscribed one, and that the rms power is half of the maximum power, the result is

$$P_{\text{rms}} = \frac{\pi t B_o^2 \omega^2 a^4}{256\rho} \quad \text{for an inscribed circle}$$
$$P_{\text{rms}} = \frac{\pi t B_o^2 \omega^2 a^4}{64\rho} \quad \text{for a circumscribed circle} \tag{C.6}$$

It is possible to approximate the total power dissipated in the test article's covering by supposing the applied field is everywhere perpendicular to the test article surface and that its amplitude is 0.5 T over the length of the rotor and zero elsewhere. The resulting losses are plotted as a function of frequency in Figure C.2.

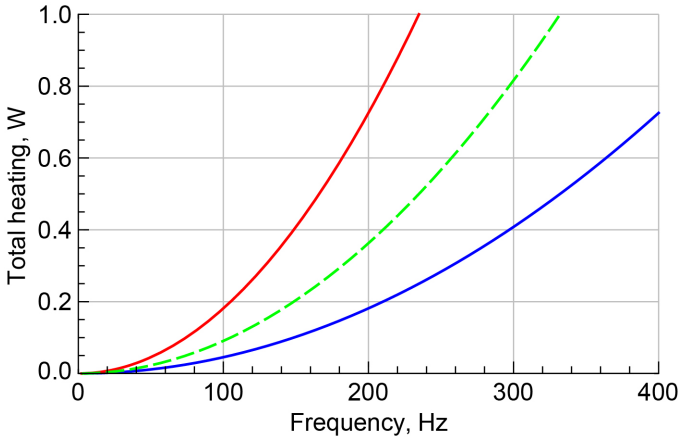

Figure C.2.—Total heating of aluminized squares on test article as function of frequency, approximated by losses in inscribed circles (blue curve) and circumscribed circles (red curve). Geometric mean between two results is green curve and may be reasonable approximation for losses in squares.

Appendix D.—Fan Characteristics and Pressure Drops in Flow Circuit

The characteristics of the fan that will drive the helium (He) flow are shown in the manual for the fan (Stirling Cryogenics: Operation and Maintenance Manual Böhmwind CryoFan). As noted in the main text, the fan produces a pressure head Δh, not a pressure difference ΔP. These are related through

$$\Delta P = \rho g \Delta h \tag{D.1}$$

where ρ is the fluid density and g is the acceleration due to gravity.

The following standard equations were used for fluid flow analysis. Pressure drop ΔP_n in each portion (designated by index n) of the fluid flow circuit was found from

$$\Delta P_n = \frac{ff_n L_n \rho v_n^2}{2 D_n} \tag{D.2}$$

where ff_n is the Darcy friction factor for section n; L_n is the length of section n; ρ is the fluid density; v_n is the fluid velocity; and D_n is the hydraulic diameter of the channel or pipe being evaluated.

The Darcy friction factor is a function of the Reynolds number Re

$$ff = \begin{Bmatrix} 0.316/\mathrm{Re}^{0.25} & \text{for Re} > 3{,}000 \\ 64/\mathrm{Re} & \text{for Re} < 3{,}000 \end{Bmatrix} \tag{D.3}$$

and the Reynolds number is given by

$$\mathrm{Re} = \frac{\rho v D}{\mu} \tag{D.4}$$

where μ is the fluid viscosity. The two expressions in the friction factor are plotted in Figure D.1.

All the GHe properties were found by using the REFPROP code available from NIST.

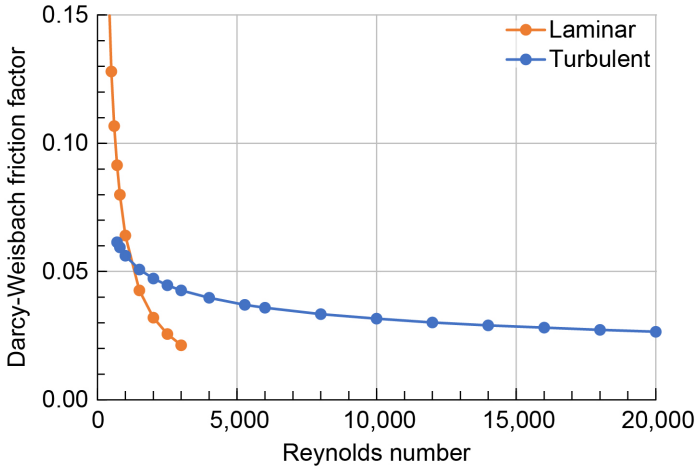

Figure D.1.—Friction factor for laminar and turbulent flow.

Appendix E.—Heat Transfer in Cooling Channels and Inlet-to-Outlet Warmup

The following equations were used to predict the heat transfer coefficient h and the superheat ΔT of the wire above the local fluid temperature.

$$
\begin{aligned}
&Q_{dot} = hA\Delta T \\
&h = \mathrm{Nu}\frac{K}{D} \\
&\mathrm{Nu1} = \frac{ff}{8}(\mathrm{Re}-1000)\frac{\mathrm{Pr}}{\left[1+12.7(ff/8)^{0.5}\left(\mathrm{Pr}^{2/3}-1\right)\right]} \qquad \text{Gnielinski} \\
&\mathrm{Nu2} = 0.023\mathrm{Re}^{0.8}\mathrm{Pr}^{0.4} \qquad \text{Dittus-Boelter} \\
&\mathrm{Nu} = \mathrm{Nu2} \\
&\mathrm{Pr} = C_p\frac{\mu}{K}
\end{aligned}
\tag{E.1}
$$

where A is an area over which heat flux is evaluated, K is the surface heat transfer coefficient, D is hydraulic diameter, Nu is the Nusselt number, C_p is heat capacity at constant pressure, and Pr is the Prandtl number. Two correlations to predict Nusselt number are compared in Figure E.1. The NASA Glenn Research Center team chose to use the Dittus-Boelter correlation. The Prandtl number for helium (He) in the range of T and P is a weak function of pressure and temperature, as shown in Figure E.2. The Prandtl number is used to find the Nusselt number, and then the heat transfer coefficient. The thermal conductivity of He in this range is weakly dependent on pressure, but it does depend on temperature as shown in Figure E.3. A representative curve of the heat transfer coefficient as a function of the velocity in the cooling channels is plotted in Figure E.4 for 4 bar and 25 K.

The warmup ΔT_{io} from inlet to outlet is found by equating the rate of enthalpy increase ΔH of the helium between inlet and outlet to the sum of the alternating current (AC) losses P_{ac} and the tare heat leak P_{tare} into the experiment pack:

$$\Delta H = vA\rho C_p \Delta T_{io} = P_{ac} + P_{\mathrm{tare}} \tag{E.2}$$

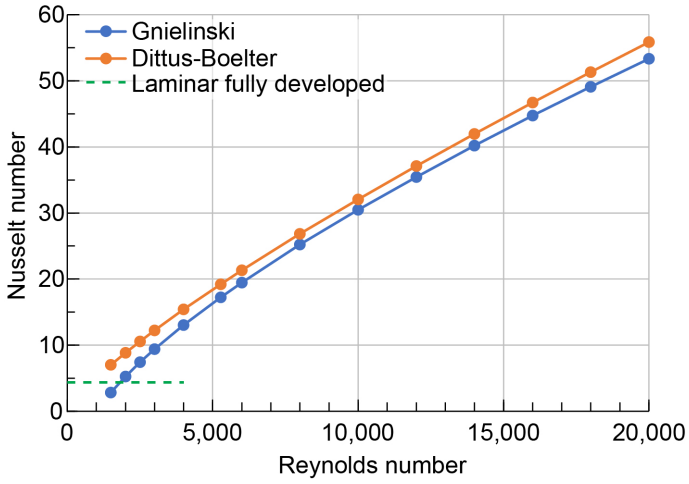

Figure E.1.—Comparison of Dittus-Boelter and Gnielinski correlations.

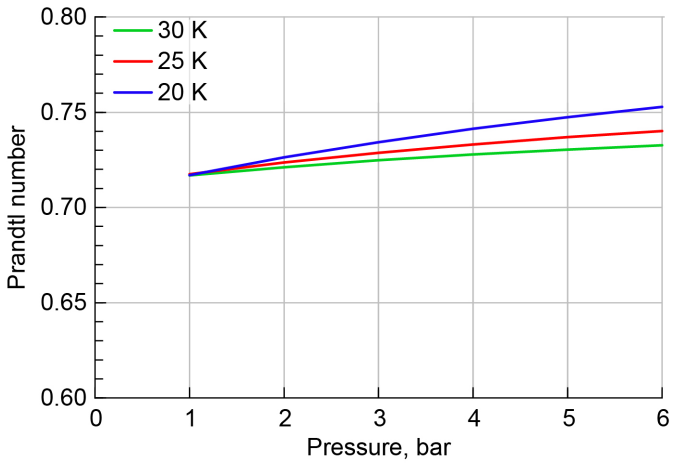

Figure E.2.—Prandtl number for He as function of temperature and pressure in range of interest.

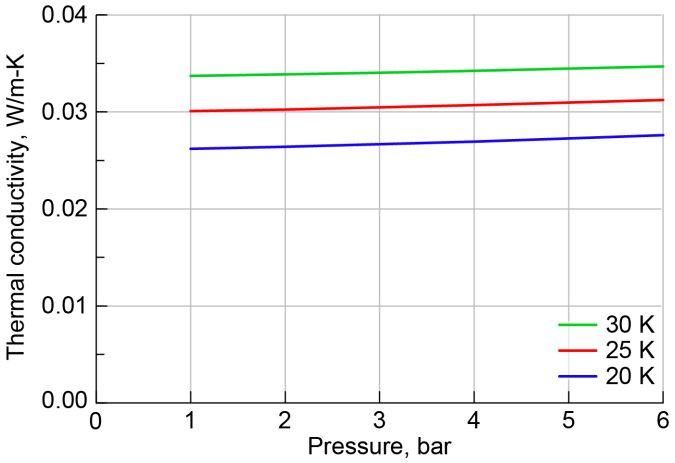

Figure E.3.—Dependence of He thermal conductivity on temperature and pressure in range of interest.

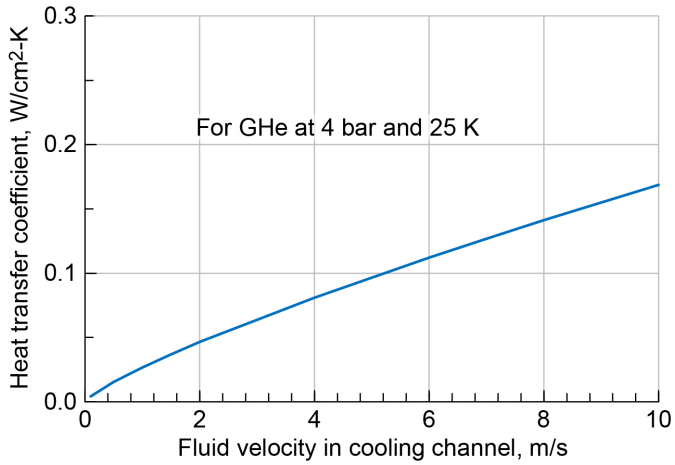

Figure E.4.—Surface-to-fluid heat transfer coefficient for He at 25 K and 4 bar.

Appendix F.—Pressure Drop, Cooldown, and Heat Transfer in Heat Exchanger

The internal details of the heat exchanger are not available at this writing. The purpose of this appendix is to determine whether the head drop in the exchanger is too high or cooldown and heat transfer too low for the system's needs. The objective is to find a model heat exchanger with the same performance as the real one.

First, let us assume that there are n parallel passages and attempt to estimate their length and hydraulic diameter from published data on head drop and thermal performance. Then, by using L and D, estimate the head drop and the heat removal capability of the model heat exchanger for the operating conditions. Using the set of fluid-flow equations from Appendix D (Eqs. (D.1) to (D.4)) and the published data for head versus flow rate, derive a relation between L, D, and n, and solve for L. Then, from the rather sparce information available on cooldown of gas in the heat exchanger, and the restriction that the total heat transferred from the fluid to the exchanger must equal the decrease in enthalpy of the fluid from inlet to outlet, get expressions for both L and D as functions of n.

Assume there are n identical, square, parallel passages of length L, hydraulic diameter D, available heat transfer area A_{ht}, and fluid velocity v. The following equations apply for turbulent flow in each passage:

$$\begin{aligned}
\Delta P &= \frac{ff\, L \rho v^2}{(2D)} \\
v &= \frac{\dot{V}_n}{D^2} \\
ff &= \frac{0.316}{\mathrm{Re}^{0.25}} \\
\mathrm{Re} &= \frac{\rho v D}{\mu} = \frac{\rho \frac{\dot{V}_n}{D}}{\mu} = \frac{\rho \dot{V}_n}{D\mu} \\
\Delta P &= \rho g \Delta Head
\end{aligned} \tag{F.1}$$

where the notation is the same as in Appendix D, ΔP is the pressure drop through each passage, and $\dot{V}_n$ is the volume flow rate through each passage. The total flow $\dot{V}_t$ through the heat exchanger is $n\dot{V}_n$. The Equation (F.1) equations can be combined and solved for L in terms of D and n. The result is

$$L = 2D\frac{\Delta P}{ff\, \rho v^2} = 6.329\frac{D^{4.75}\ \rho^{0.25} g}{\mu^{0.25}}\frac{\Delta Head}{\dot{V}_n^{1.75}} \tag{F.2}$$

From a curve fit to the data for head loss versus total flow rate at 30 K and 20 bar in the heat exchanger manufacturer's user manual, obtain the following relation:

$$\Delta Head = 1.07 * 10^7\ \dot{V}_t^{1.75} \text{ (at 30 K and 20 bar)} \tag{F.3}$$

Then, noting that at 30 K and 20 bar, $\rho = 30.75$ kg/m^3, and $\mu = 5.147\times10^{-6}$ Pa-s, obtain

$$L\ = 3.28 * 10^{10} D^{4.75} * n^{1.75} \tag{F.4}$$

which is independent of temperature and pressure.

Next, find another relation between L and D from Vermuelen (2013), which indicates that the heat exchanger can remove 100 W from He entering at 35 K and leaving at 33 K if the heat exchanger is at 32 K. Note that the mean temperature difference between the gas and the heat exchanger will be 2 K for these conditions. From that information, the He flow rate required to reject 100 W can be found (as well as the second relation between L, D, and n) from the rate of heat transfer from the fluid to the heat exchanger. The total volume flow rate, $n\dot{V}_n$, can be found from

$$n\dot{Q}_{\text{cool}} = \rho n \dot{V}_n C_p \Delta T_{\text{in-out}} = 100 \text{ W} \tag{F.5}$$

where $\dot{Q}_{\text{cool}}$ is the amount of heat rejected from gas to exchanger in each passage. The required total flow rate is found to be 1.221 m^3/h for this situation.

The additional relation between L, D, and n is found from the fact that 100 W must also be transferred from the gas to the heat exchanger. The following relations are applied to each individual passage:

$$\begin{aligned}
&\dot{Q}_{ht} = hA_{ht}\Delta T_{ht} \\
&h = \text{Nu}\frac{K}{D} \\
&A_{ht} = L4D = 4LD \\
&\text{Nu} = 0.023\,\text{Re}^{0.8}\,\text{Pr}^{0.4} \quad \text{(Dittus-Boelter)} \\
&\text{Re} = \frac{\rho \dot{V}_n}{D\mu}
\end{aligned} \tag{F.6}$$

Combining these relations yields

$$\dot{Q}_{ht} = 0.092\frac{\rho \dot{V}_n}{(D\mu)^{0.8}}\text{Pr}^{0.4} KL\Delta T_{ht} = \frac{100}{n} \quad \text{(20 bar, 34 K)} \tag{F.7}$$

Substituting the known values of $n\dot{V}_n$, ΔT_{ht}, and helium (He) properties at 20 bars and 34 K, and solving for L yields

$$L = 39.56\frac{D^{0.8}}{n^{0.2}} \tag{F.8}$$

From this relation plus the previous one for L in terms of D and n, we can obtain expressions for D and L in terms of n:

$$D = \frac{0.005522}{n^{0.4937}} \text{ and } L = \frac{0.6179}{n^{0.5949}} \tag{F.9}$$

Representative values of n, D, and L for equivalent model heat exchangers are shown in Table F.1.

According to the equations that have been used for analysis, a heat exchanger constructed with the combination of n, D, and L shown in any one row of Table F.1 will have pressure drop and heat transfer that matches the data used in this derivation. Going further, any row can now be used to predict the pressure drop and heat transfer in the actual heat exchanger for any other set of conditions, as long as the flow remains turbulent.

TABLE F.1.—CALCULATED HYDRAULIC DIAMETER AND PASSAGE LENGTH AS FUNCTIONS OF NUMBER OF PARALLEL PASSAGES

n	D, m	L, m
1	0.00552	0.618
2	0.00392	0.409
4	0.00279	0.271
8	0.00198	0.179
16	0.00140	0.119
32	0.00100	0.079
64	0.00071	0.052

First, however, we check that the derived relations reproduce the data from which they were derived.

F.1 Head Loss Check

Using these equations for L and D and the head loss equations above, the predicted head loss is seen in Figure F.1 to accurately reproduce the data taken from the vendor graph.

F.2 Heat Transfer and Cooldown Check

Using these equations for L and D at the flow rate (1.221 m^3/h), at 20 bar and 34 K used by Vermuelen (2013), the heat transfer relations correctly predict 100 W of heat transfer rate from the gas to the heat exchanger and also 100 W of enthalpy loss rate from the He between inlet and outlet for any chosen value of n.

It is now possible to predict the head loss and the heat removal capability of the heat exchanger for any other temperature, pressure, and flow rate of interest. For a rough comparison with tabulated values in Table 2, we choose 25 K and 4 bar as the conditions of the He at the midpoint in the heat exchanger. Suppose that the heat exchanger temperature is at 22 K, giving an average ΔT_{ht} for heat exchange of 3 K. The outlet difference in temperature between the gas and exchanger and the cooldown from inlet to outlet varies with flow rate. Some results for a range of flow rates are displayed in Figure F.2, where the head drop curve in blue is read on the right scale. For the flow rate used in Table 2 (0.551 m^3/h), the head drop is predicted to be only 3.1 m, which is minor compared to the head drop expected in the rest of the system. The two heat removal rates are on the order of 27 W, which would cover the 5-mm twist-pitch cases in Table 2, if there were no other heat inputs but would be considerably short of the heat produced in the three 10-mm cases. Populating only one side of the sample holder in the 10-mm twist pitch case would bring the heat generated in the experiment into the rejectable range. It may be noted that the existing cryocooler has a lift capacity at 22 K of about 70 W, so it can easily absorb 27 W. In fact, it would require resistive heat to be added to hold the heat exchanger temperature at 22 K.

Increasing the charging pressure of the He system to 6 bar gives the results in Figure F.3, which shows that 37 W could be absorbed at the 0.551 m^3/h flow rate. Dropping the cold head temperature to 21 K would allow 50 W to be absorbed at that flow rate. For situations that may arise where still more heat must be removed, it would be possible to add a second fan, a second cryocooler, or both to the circuit. Redesigning the test article for a pressure higher than 6 bar would be beneficial as well.

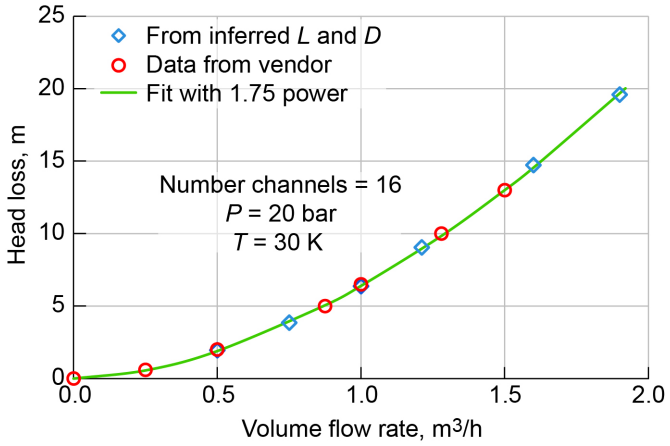

Figure F.1.—Head loss from experimental data and from inferred heat exchanger parameters.

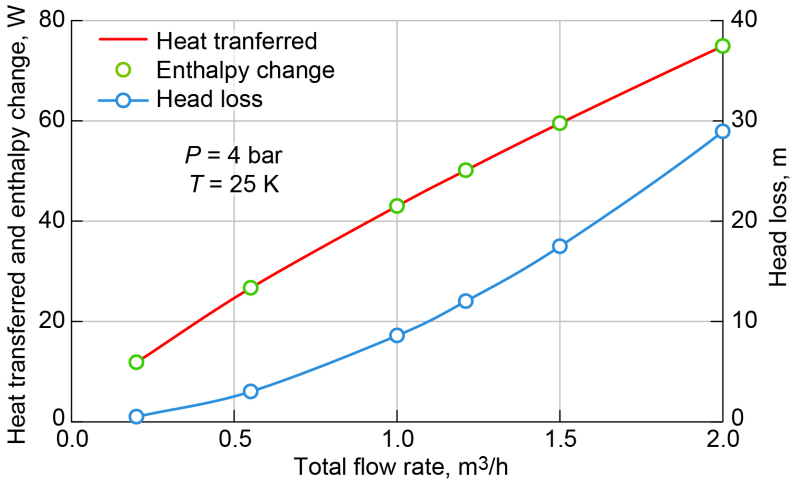

Figure F.2.—Heat transfer, cooling, and head loss as functions of He flow rate at 4 bar.

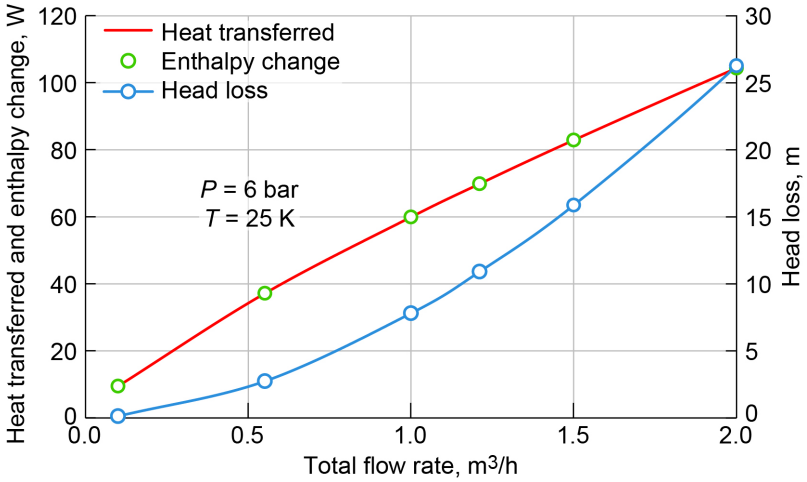

Figure F.3.—Heat transfer, cooling, and head loss as functions of He flow rate at 6 bar.

References

Brown, Gerald, et al. (2020): Status of Analysis and Manufacturability of Superconducting Wires With Low AC Losses. NASA/TM-20205005815. http://ntrs.nasa.gov.

Carr, W.J., Jr. (2001): AC Loss and Macroscopic Theory of Superconductors. Second ed., Taylor & Francis, New York, NY.

Hartwig, Jason, et al. (2019): New Test Rig to Measure Alternating Current Losses of Both Low and High Critical Temperature Superconductors. NASA/TM—2019-220046. http://ntrs.nasa.gov

Haugan, Timothy J. (2015): Superconductivity Research at AFRL: Superconducting Coils in Rotating Magnetic Fields. Joint Quantum Electronic Solids and GHz-THz Electronics AFOSR Program Review, March 24, 2015, Arlington, VA, unpublished.

Hyper Tech Research, Inc. (2013): Low AC-Loss Magnesium Diboride Superconductors for Turbo-Electric Aircraft Propulsion Systems. Contract No. NNX13CC20P SBIR Phase I Final Technical Report, November 22, 2013, unpublished.

Hyper Tech Research, Inc. (2019): Fine-Filament Magnesium Diboride Superconductor Wire for Turboelectric Propulsion Systems (Prototype AC Superconducting Stator Coils). Contract Number NNX14CC11C, Phase IIX Final Technical Report, Aug. 26, 2019, unpublished.

Lorin, Clement; and Masson, Philippe J. (2013): Numerical Analysis of the Impact of Elliptical Fields on Magnetization Losses. IEEE Trans. Appl. Supercond., vol. 23, no. 3, article 8201405.

Murphy, John P., et al. (2013): Experiment Setup for Calorimetric Measurements of Losses in HTS Coils Due to AC Current and External Magnetic Fields. IEEE Trans. Appl. Supercond., vol. 23, no. 3, article 4701505.

Murphy, John P. (2015): Calorimetric Measurements of AC Losses in HTS Tapes in a Stator Environment. Presented at the Cryogenic Engineering Conference/International Cryogenic Materials Conference, Tucson, AZ.

Murphy, J.P., et al. (2017): AC Loss in YBCO Coated Conductors at High dB/dt Measured Using a Spinning Magnet Calorimeter (Stator Testbed Environment). Cryogenics, vol. 86, pp. 57–69.

Pamidi, Sastry, et al. (2007): Variable Temperature Total AC Loss and Stability Characterization Facility. IEEE Trans. Appl. Supercond., vol. 17, no. 2, pp. 3179–3182.

Pamidi, Sastry, et al. (2016): Variable Temperature Total AC Loss Measurements in Simultaneously Rotating and Pulsating Magnetic Field. Poster paper 2LPo1B-08, Applied Superconductivity Conference 2016, unpublished.

Stirling Cryogenics BV (2019): Manual: Heat Exchanger With Connections for Cryomech AL330. Document ID 609552 24.

Stirling Cryogenics BV (2018).: Operation and Maintenance Manual Bohmwind CryoFan. Document ID 609535 30.

Vermuelen, Harrie (2013): Cryogenic Circulators: The Solution for Cooling Problems? Cold Facts, vol. 29, pp. 46–48.